

# Quasi-Gaussian probability density function of sea wave slopes from near nadir Ku-band radar observations

Ping Chen, Gang Zheng, Danièle Hauser, Fei Xu

► **To cite this version:**

Ping Chen, Gang Zheng, Danièle Hauser, Fei Xu. Quasi-Gaussian probability density function of sea wave slopes from near nadir Ku-band radar observations. *Remote Sensing of Environment*, Elsevier, 2018, 217, pp.86 - 100. 10.1016/j.rse.2018.07.027 . insu-01856646

**HAL Id: insu-01856646**

**<https://hal-insu.archives-ouvertes.fr/insu-01856646>**

Submitted on 17 Nov 2019

**HAL** is a multi-disciplinary open access archive for the deposit and dissemination of scientific research documents, whether they are published or not. The documents may come from teaching and research institutions in France or abroad, or from public or private research centers.

L'archive ouverte pluridisciplinaire **HAL**, est destinée au dépôt et à la diffusion de documents scientifiques de niveau recherche, publiés ou non, émanant des établissements d'enseignement et de recherche français ou étrangers, des laboratoires publics ou privés.

# Quasi-Gaussian Probability Density Function of sea wave slopes from Near Nadir Ku-Band Radar Observations

*Ping Chen<sup>1,4</sup>, Gang Zheng<sup>2</sup>, Danièle Hauser<sup>3</sup>, Fei Xu<sup>1,4</sup> \**

<sup>1</sup>School of Electronic Information and Communications, Huazhong University of Science & Technology, Wuhan 430074, Hubei, China

<sup>2</sup>Second Institute of Oceanography, State Oceanic Administration, Hangzhou

<sup>3</sup>Université de Versailles Saint-Quentin-en-Yvelines, Université Paris 06, CNRS, LATMOS-IPSL, Guyancourt, France

<sup>4</sup>Science and Technology on Multi-spectral Information Processing Laboratory

---

## Abstract

1 Although in most circumstances, sea wave slope probability density function (PDF) is ex-  
2 pressed as Gaussian distribution, there is evidence that it follows quasi-Gaussian distribution,  
3 which can be represented by Gram-Charlier series to fourth order. All the statistical pa-  
4 rameters of slope PDF have previously been derived by using optical methods in specular  
5 conditions, and values and relationships with surface parameters have been presented in the  
6 literature. However they may not be relevant at microwave wavelengths due to diffraction  
7 effects. Up to now, sea surface slope PDF consistent with ocean microwave remote sensing  
8 is not known yet. So it is important to establish the parameter models of quasi-Gaussian  
9 slope PDF compatible with radar application. In this paper, based on the backscattering  
10 coefficients from the Ku-band space-borne radar Precipitation Radar (PR) data, all the pa-  
11 rameters of the quasi-Gaussian slope PDF are inverted using a so-called “GO4” ([Boisot et al.](#)  
12 [\(2015\)](#)) model with a two-dimensional (2-D) non-linear least square fit on the backscattering  
13 coefficients. We also establish the empirical formulae relating the statistical parameters of  
14 the quasi-Gaussian sea slope PDF with wind speed, which may be used for ocean Ku-band  
15 radar application.

16 The proposed empirical formulae are compared to the [Cox and Munk \(1954\)](#)-CM slope  
17 parameter model: the results confirm that the slope variance in upwind and crosswind

---

\*Correspondence author: Fei Xu, Email: xufei\_hust@163.com

18 directions as well as the skewness coefficients exhibit intermediate values between the CM  
19 slope parameters of clean surface and slick surface cases. The coefficients of peakedness are  
20 just in the range of the CM slope peakedness parameter values.

21 The impacts of wave conditions (swell or wind sea) on slope PDF parameters are also  
22 studied. The results show that in most wind speed conditions, the presence of swell increases  
23 the skewness coefficients, while it decreases the peakedness coefficients.

*Keywords:* slope probability density function of sea surface, Ku-band radar, near-nadir  
radar cross-sections, approximate scattering model

---

## 1. Introduction

24 Ocean surface waves are a topic of active research within physical oceanography, due to  
25 their role in the coupled ocean/atmosphere system and to their impact on various society  
26 sectors (national defense, navigation, shipbuilding and offshore industry...). The distribu-  
27 tion of wave slopes is an important statistical tool in describing ocean surface waves, because  
28 it is related to a number of physical processes which occur at or near the air-sea interface,  
29 such as the dynamics including wave breaking and the nonlinear energy transfer between  
30 wavenumbers, which is a strong function of both the energy-containing and high frequency  
31 waves (see *e.g.* Longuet-Higgins (1978); Om (1985); Resio and Perrie (1991)). The distri-  
32 bution of wave slopes is an important quantity in the processes of wave generation, wave  
33 growth or dissipation as well as air/sea interactions.

34 Due to the random nature of sea wave, the slope probability density function (PDF) is  
35 usually used to represent the wave slopes. The scattering of acoustic and electromagnetic  
36 waves in the optical or microwave domains is closely related to the wave slope PDF.

37 In the optical domain, the sea surface scattering can be considered as specular, which  
38 leads to a linear relationship with the slope PDF based on geometrical optics (GO) analyti-  
39 cal approximations. There are historical and more recent results presented in the literature  
40 Jackson et al. (1992); Cox and Munk (1954, 1956) which are based on this property to esti-  
41 mate the surface slope PDF at optical wavelengths. Based on the analysis of sun glitter on

42 the sea surface, [Cox and Munk \(1954\)](#) used the geometrical optics approximation combined  
43 with the assumption that sea surface slope PDF is quasi-Gaussian and can be expressed  
44 by a Gram-Charlier expansion up to the fourth order, where the slope variances, skewness  
45 coefficients and peakedness coefficients are included. They established empirical formulae  
46 relating the seven parameters of the slope PDF approximated by the Gram-Charlier expan-  
47 sion, to wind speed. [Br on and Henriot \(2006\)](#) used visible light reflection data provided  
48 by POLDER multiple angular radiometer carried on the ADEOS-1 satellite and wind data  
49 from the NSCAT wind scatterometer to invert the same parameters under various wind  
50 speed conditions and to revisit the empirical formulae proposed by Cox and Munk. In these  
51 studies, it was assumed that the slope PDF is only related to wind speed.

52 However, these results obtained from optical measurements cannot be transposed directly  
53 in the application of ocean microwave remote sensing because of the diffraction effects at  
54 wavelengths longer than optical ones. So it is important to establish the parameter models  
55 of quasi-Gaussian slope PDF for radar application. This is the aim of our work.

56 In the microwave domain, at low incidence (*i.e.*, near-nadir incidence) the sea surface  
57 scattering can be considered as quasi-specular, the geometrical optics (GO) approxima-  
58 tion still holds if one considers the diffraction-modified Fresnel reflectivity ([Tsang and Kong](#)  
59 [\(2001\)](#)) and the slope PDF of surfaces waves only for waves longer than the diffraction limit  
60 ([Jackson et al. \(1992\)](#); [Barrick \(1968\)](#)). This motivated the introduction and use of the notion  
61 of radar-filtered slope statistics by several authors [Jackson et al. \(1992\)](#); [Tsang and Kong](#)  
62 [\(2001\)](#); [Barrick \(1968\)](#); [Hauser et al. \(2008\)](#); [Boisot et al. \(2015\)](#); [Freilich and Vanhoff \(2003\)](#);  
63 [Chu et al. \(2012a\)](#). The following paragraphs give the review of these studies. In [Jackson et al.](#)  
64 [\(1992\)](#), [Freilich and Vanhoff \(2003\)](#) such filtered sea slope PDF is assumed Gaussian and fil-  
65 tered slope variances is studied, while in [Hauser et al. \(2008\)](#), [Chu et al. \(2012a\)](#) such sea  
66 slope PDF is assumed quasi-Gaussian, however, due to the limits of both the scattering  
67 model and the inversion method, not all parameters in the slope PDF can be obtained. This  
68 furthermore motivates us to study the approximation scattering model at low incidence with  
69 high accuracy, as well as the inversion method, then to find all the seven parameters in a

70 quasi-Gaussian filtered” slope PDF, and establish the parameter models of quasi-Gaussian  
71 slope PDF for radar application.

72 Results on the slope PDF estimated from microwave observations have also been pre-  
73 sented in the literature [Boisot et al. \(2015\)](#); [Freilich and Vanhoff \(2003\)](#); [Tsang and Kong](#)  
74 [\(2001\)](#); [Hauser et al. \(2008\)](#). With the assumption of a Gaussian slope PDF and observa-  
75 tions very close to nadir it is admitted that the filtering occurs below three to five times  
76 the radar wavelength. However, this may vary with incidence range and with roughness  
77 conditions.

78 With the assumption of isotropy (the slope variance in upwind equals that in crosswind)  
79 and a Gaussian slope PDF, [Jackson et al. \(1992\)](#) averaged the backscatter coefficients at  
80 different azimuth from the Ku-band airborne-spectrometer ROWS (incidences of 0-20°), and  
81 derived the slope variances from a one-dimensional (1-D) inversion method. He established  
82 empirical formulae for the variation of slope variances with wind speed applicable for Ku-  
83 band observations. The same method was used later ([Freilich and Vanhoff \(2003\)](#)) on a  
84 larger data set by using Tropical Rainfall Mapping Mission (TRMM) data of Precipitation  
85 radar (PR) in the 0-18° incidence range co-located with wind estimates from the TRMM  
86 microwave Imager.

87 [Hauser et al. \(2008\)](#) analyzed 2-D backscattering coefficients (as a function of incidence  
88 and azimuth) at C-band from the airborne-spectrometer STORM to derive the slope vari-  
89 ances in upwind and crosswind directions as well as a peakedness parameter based on the  
90 compound model of slope PDF by [Chu et al. \(2012a\)](#). However, because the inversion was  
91 applied independently for each azimuth observation, the skewness coefficients, which are  
92 related to the anisotropic properties of slope PDF, were not studied.

93 [Chu et al. \(2012a\)](#) used the backscattering coefficients from the Precipitation Radar (PR)  
94 of Tropical Rainfall Mapping Mission (TRMM) co-located with wind information from buoys  
95 to invert the slope variance in upwind and crosswind directions and two skewness coefficients  
96 under various wind speeds. They used the heuristic inversion method also used by Cox and  
97 Munk. Their results show that the asymmetry of backscattering between downwind and

98 upwind at low incidence is caused by the skewness of wave slope PDF. However, three  
99 coefficients of peakedness have not been estimated in their study. Therefore, the complete  
100 relationships between the seven parameters of the quasi-Gaussian sea wave slope PDF and  
101 wind speed have not been established for microwave band until now.

102 Besides optical and microwave methods, [Vandemark et al. \(2004\)](#) estimated slope PDF  
103 by using direct range measurements with an airborne laser, but the approach provides infor-  
104 mation only in a non-directional sense, and for waves longer than about 2 m in wavelength.  
105 [Shaw and Churnside \(1997\)](#); [Hwang and Wang \(2004\)](#) and [Hwang \(2005\)](#) made in situ spec-  
106 tral measurements of ocean waves from a free-drifting buoy and estimated the variance of  
107 the slope PDF of ocean waves whose wavelength are in the range of about 0.02-6 m.

108 In the references mentioned here-above the inversion of the slope PDF from data set  
109 in the microwave band is based on the Quasi-Specular (QS) model, *i.g.*, the GO scattering  
110 model with filtered slope statistic parameters and the diffraction-modified Fresnel reflectivity.  
111 However, QS model accuracy is only of the order of several percent in [Hauser et al. \(2008\)](#) at  
112 low incidence angles, if compared with the Physical Optics model (PO), which is considered  
113 as the reference model at near-nadir incidences. For the case of Gaussian slope PDF, the QS  
114 model accuracy does not affect significantly the inversion results on slope variances because  
115 the inversion of Gaussian slope PDF is a kind of linear inversion. In contrast, for the case  
116 of quasi-Gaussian slope PDF where the aim is to invert higher order parameters of the  
117 slope statistics, such as peakedness and skewness coefficients, the effect of curvature must  
118 be taken into account by [Bringer et al. \(2012\)](#); [Boisot et al. \(2015\)](#). So QS model accuracy  
119 is not enough for this case since the curvature effect is ignored in QS model.

120 [Bringer et al. \(2012\)](#) developed a GO4 model by using the 4th order expansion (instead of  
121  $2^{nd}$  order expansion in GO) of the structure function which appears in the Kirchhoff integral  
122 of the PO model to take the effect of curvature into account. In their model, both slope  
123 and curvature parameters are considered as total and the model agrees well in the first few  
124 degrees of incidence with PO. However, ignoring the filtering effect on slope and curvature  
125 variances for microwave band results in a decrease of model accuracy as the incidence angle

126 increases. [Boisot et al. \(2015\)](#) improved the interpretations for the parameters of the GO4,  
127 *i.g.*, only slope parameters are considered total while the curvature parameters is regarded  
128 as filtered. With the improvement, the accuracy of GO4 in [Boisot et al. \(2015\)](#) is increased  
129 relative to that of the former version of GO4 presented in [Bringer et al. \(2012\)](#).

130 In this paper, we use the same model GO4 and we will show in a first part (Section  
131 2) that in opposite to the results of [Boisot et al. \(2015\)](#) and [Bringer et al. \(2012\)](#), we must  
132 invoke parameters of the surface slope PDF filtered at a certain scale to reproduce with a  
133 high accuracy the PO model. In opposite to [Boisot et al. \(2015\)](#) and [Freilich and Vanhoff](#)  
134 [\(2003\)](#) our approach takes into account the anisotropic nature of the surface (variations with  
135 azimuth angle). Then, using the TRMM/Precipitation Radar (PR) data set co-located with  
136 buoy measurements, the dependence of the backscattering coefficients with both incidence  
137 and azimuth angles are analyzed. By applying a non-linear fit of the GO4 model to the  
138 observations, all the seven coefficients of the Gram-Charlier expansion of a quasi -Gaussian  
139 slope PDF are inverted under different wind speeds; furthermore, empirical formulae relating  
140 each of the seven parameters with wind speed are proposed for the first time for Ku-band.

141 The paper is organized as follows. In section 2.1, we introduce the scattering model  
142 (GO4) used for estimating the parameters of the quasi-Gaussian slope PDF from the nor-  
143 malized radar cross-sections. In Section 2.2, we analyze the results of GO4 inversion applied  
144 on backscatter simulations. The reference of the simulation are normalized radar cross-  
145 sections calculated from the PO model and a standard surface description (wave spectrum  
146 from [Elfouhaily et al. \(1997\)](#) in a wind sea case, and mixed sea case with wind sea and  
147 swell). This part allows us to assess the range of incidence and wind conditions in which the  
148 differences between GO4 and PO are minimum. Simulations are also used to estimate the  
149 cut-off wavelength of the inverted parameters. Section 3 briefly describes the data set used  
150 in the present analysis (PR observations from the TRMM satellite). Section 4 presents the  
151 results obtained from the inversion of the PR data set, and provides comparison with the  
152 [Cox and Munk \(1954\)](#)-CM- model. Then, empirical formulas for the seven effective param-  
153 eters of slope PDF with wind speed are summarized. The main results are summarized in

154 the conclusion.

## 155 2. Slope PDF Inversion Model and Method

### 156 2.1. Scattering Model

157 At near-nadir incidence angles, the PO scalar approximation is considered accurate  
158 enough as long as polarization effects remain negligible, that is in the first 20-25° inci-  
159 dence away from nadir by [Thompson et al. \(2005\)](#). In the following, PO is referred to as  
160 the reference model, and other models mentioned are all approximation models. Indeed, to  
161 overcome the limitations of the classical GO model, as well as QS model, [Boisot et al. \(2015\)](#)  
162 and [Bringer et al. \(2012\)](#) proposed an alternative approximation called GO4, to take into  
163 account possible deviation of the surface from the approximate tangent plane. The main idea  
164 proposed in [Boisot et al. \(2015\)](#) and [Bringer et al. \(2012\)](#) was to make use of the 4th order  
165 expansion (instead of 2<sup>nd</sup> order expansion in GO) of the structure function which appears in  
166 the Kirchhoff integral of the PO model ([Boisot et al. \(2015\)](#)). Both the slope and curvature  
167 variances in GO4 in [Bringer et al. \(2012\)](#) are total. Compared with GO4 in [Bringer et al.](#)  
168 [\(2012\)](#), the improvement of GO4 in [Boisot et al. \(2015\)](#) is that the curvature variances are  
169 considered as filtered. GO4 in [Boisot et al. \(2015\)](#) express the normalized radar cross-section  
170 (NRCS) in the isotropic case as [Boisot et al. \(2015\)](#):

$$171 \sigma_{GO4}^0(\theta, \varphi) = \frac{|R|^2}{mss} \sec^4(\theta) \exp\left(-\frac{\tan^2(\theta)}{mss}\right) \times \quad (1)$$
$$\left[1 + \frac{msc_e}{16K^2 mss^2 \cos^2 \theta} \left(\frac{\tan^4(\theta)}{mss^2} - 4\frac{\tan^2(\theta)}{mss} + 2\right)\right]$$

172 where  $R$  is the Fresnel reflectivity,  $\theta$  the incidence angle,  $mss$  the total mean square slope  
173 and  $msc_e$  the filtered mean square curvature of the sea surface. This equation was derived  
174 in [Boisot et al. \(2015\)](#) by considering that the  $msc$  value is relative to a filtered surface and  
175  $msc_e$  can be determined with the use of additional PO NRCS at incidence 0° (and only at  
176 this incidence).



177 In the anisotropic case, Eq.(1) becomes:

$$\begin{aligned}
 \sigma_{GO4}^0(\theta, \varphi) = & \frac{|R|^2}{2\sqrt{mssx}\sqrt{mssy}} \sec^4(\theta) \exp\left(-\frac{1}{2}(X^2+Y^2)\right) \times \\
 & \left\{ 1 + \frac{1}{96K^2\cos^2\theta} \left[ \begin{aligned} & \frac{6mscopy_e}{mssx \cdot mssy} H_2(X)H_2(Y) \\ & + \frac{mssc_x}{mssx^2} H_4(X) + \frac{mssc_y}{mssy^2} H_4(Y) \end{aligned} \right] \right\} \quad (2)
 \end{aligned}$$

179 where  $mssx$  and  $mssy$  are total mean square slopes in two orthogonal directions,  $mssc_x$ ,  
 180  $mssc_y$ , and  $mscopy$  are directional curvatures,  $H_n$  is the Hermitte polynomials of order  $n$  and  
 181  $X$  and  $Y$  defined as:

$$H_n(u) = (-1)^n e^{\frac{u^2}{2}} \frac{d^n}{du^n} e^{-\frac{u^2}{2}}, X = \frac{\tan\theta \cos\varphi}{\sqrt{mssx_e}}, Y = \frac{\tan\theta \sin\varphi}{\sqrt{mssy_e}} \quad (3)$$

183 Here we use the same models, but instead of imposing this constraint,  $mss$ ,  $mssc$  and  $R$  in  
 184 Eq.(1) and  $mssx$ ,  $mssy$ ,  $mssc_x$ ,  $mssc_y$ ,  $mscopy$ , and  $R$  in Eq.(2) are obtained by directly fitting  
 185 Eq.(1) or Eq.(2) to PO  $\sigma^0$  over a chosen incidence range. We will show below (see section  
 186 2.2), that in fact the variable  $mss$ ,  $mssc$ ,  $mssx$ ,  $mssy$ ,  $mssc_x$ ,  $mssc_y$  and  $mscopy$  obtained by such  
 187 fitting are relative to the filtered surface, and  $R$  is also a diffraction-modified coefficient.

188 We recall by comparison, that the QS model under the assumption of Gaussian statistics  
 189 of the surface writes:

$$\sigma_{QS}^0(\theta, \varphi) = \frac{|R_e|^2}{2\sqrt{mssx_e}\sqrt{mssy_e}} \sec^4(\theta) \exp\left(-\frac{1}{2}(X^2 + Y^2)\right) \quad (4)$$

191 Where both  $mssx_e$  and  $mssy_e$  are filtered mean square slopes, and  $R_e$  is also a diffraction-  
 192 modified coefficient.

193 In Eq.(1-3), the surface was considered as Gaussian. In reality, as shown in Cox and Munk  
 194 (1956, 1954), the ocean surface is a weakly non-Gaussian surfac, and the Gram-Charlier se-  
 195 ries developed to the fourth order can be used to express such a quasi-Gaussian sea slope

196 PDF:

$$\begin{aligned}
 p(X, Y) = & \frac{1}{2\pi\sqrt{mssx}\sqrt{mssy}} \exp\left(-\frac{1}{2}(X^2+Y^2)\right) \times \left[1 + \frac{\lambda_{12}}{2} H_2(Y)H_1(X) + \right. \\
 & \left. \frac{\lambda_{30}}{6} H_3(X) + \frac{\lambda_{22}}{4} H_2(Y)H_2(X) + \frac{\lambda_{40}}{24} H_4(X) + \frac{\lambda_{04}}{24} H_4(Y)\right]
 \end{aligned} \tag{5}$$

197  
198 Where  $\lambda_{12}$ ,  $\lambda_{30}$  are skewness coefficients for sea surface slope,  $\lambda_{22}$ ,  $\lambda_{40}$  and  $\lambda_{04}$  are peaked-  
199 ness coefficients for sea surface slope.

200 The skewness and kurtosis parameters are related to the structure function of the 3rd and  
201 4th order in PO by [Thompson et al. \(2005\)](#). Using the definition of the structure functions  
202 and expanding them to the third order and the fourth order, they can be approximated for  
203 small arguments by:

$$\begin{aligned}
 S_3(x, y) & \approx \lambda_{30}mssx^{3/2}x^3 + 3\lambda_{12}mssx\sqrt{mssy}xy^2 \\
 S_4(x, y) & \approx \lambda_{40}mssx^2x^4 + \lambda_{04}mssy^2y^4 + 6\lambda_{22}mssx \cdot mssy \cdot x^2y^2
 \end{aligned} \tag{6}$$

204  
205 where the dimensionless coefficients  $\lambda_{mn}$  are defined by

$$\lambda_{mn} = \frac{\langle (\partial_x \eta)^m (\partial_y \eta)^n \rangle}{\langle (\partial_x \eta)^2 \rangle^{m/2} \langle (\partial_y \eta)^2 \rangle^{n/2}} \tag{7}$$

206  
207 With these assumptions, [Boisot et al. \(2015\)](#) expressed the NCRS of the GO4 model for  
208 quasi-Gaussian sea surface. They obtained the following equation:

$$\begin{aligned}
 \sigma_{GO4}^0(\theta, \varphi) = & \frac{|R|^2}{2\sqrt{mssx}\sqrt{mssy}} \sec^4(\theta) \exp\left(-\frac{1}{2}(X^2 + Y^2)\right) \times \\
 & \left\{ 1 + \frac{1}{24Q_z^2} \left[ \begin{aligned} & 6 \left( \frac{msscxy_e}{mssx \cdot mssy} + \lambda_{22}Q_z^2 \right) H_2(X)H_2(Y) \\ & + \left( \frac{mssc_x}{mssx^2} + \lambda_{40}Q_z^2 \right) H_4(X) \\ & + \left( \frac{mssc_y}{mssy^2} + \lambda_{04}Q_z^2 \right) H_4(Y) \end{aligned} \right] \right. \\
 & \left. + \frac{1}{6} [3\lambda_{12}H_1(X)H_2(Y) + \lambda_{30}H_3(X)] \right\}
 \end{aligned} \tag{8}$$

209  
210 where  $Q_z$  is twice the radar wavenumber projected in the vertical direction.

211 In the development of [Boisot et al. \(2015\)](#) the mean square slope parameters are supposed  
212 to be non-filtered parameters whereas the curvature parameters are filtered parameters. We

213 will see in section below that in fact, all parameters in Eq.(8) related to slope and curvature  
 214 are filtered parameters, and that  $R$  is a diffraction-modified reflection coefficient.

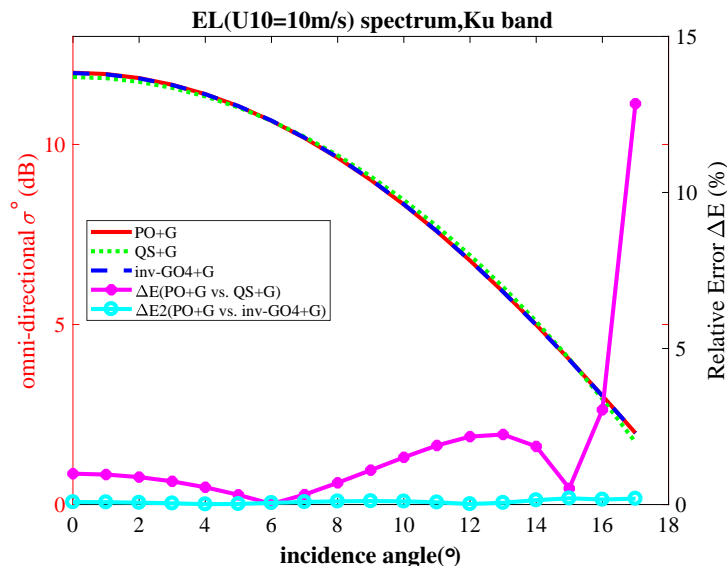


**Fig. 1.**  $\sigma^\circ(\theta)$  (in dB) as a function of  $\theta$  with the PO model (red line) for a 10 m/s wind speed, using EL spectrum, for Ku-band, and after averaging  $\sigma^\circ(\theta, \varphi)$  in all azimuths. The results from the fit of the GO4 and QS model are shown with the dotted blue and green lines, denoted by inv-GO4 and QS, respectively. Curve with dots represent relative errors between PO and inv-GO4 (cyan), between PO and QS (magenta), respectively.

215 We recall here for comparison with Eq.(8), that the QS model in the case of a quasi-  
 216 Gaussian surface writes:

$$\begin{aligned}
 \sigma_{QS}^0(\theta, \varphi) = & \frac{|R_e|^2}{2\sqrt{m_{ss}x_e}\sqrt{m_{ss}y_e}} \sec^4(\theta) \exp\left(-\frac{1}{2}(X^2+Y^2)\right) \times \\
 & \left[1 + \frac{\lambda_{12}}{2}H_1(X)H_2(Y) + \frac{\lambda_{30}}{6}H_3(X) + \frac{\lambda_{22}}{4}H_2(Y)H_2(X) + \frac{\lambda_{40}}{24}H_4(X) + \frac{\lambda_{04}}{24}H_4(Y)\right]
 \end{aligned} \tag{9}$$

## 218 2.2. Conditions for GO4 inversion determined by simulations

219 Before using GO4 to invert real data, we tested the ability of the model to reproduce, in  
 220 the Gaussian case, the PO physical model results and we compared the results with  $\sigma^\circ$  of  
 221 QS model in Jackson et al. (1992) (as well as Freilich and Vanhoff (2003), Chu et al. (2012a),  
 222 Hauser et al. (1992), Jackson et al. (1985), Hesany et al. (2000), Caudal et al. (2005), Longuet-higgins

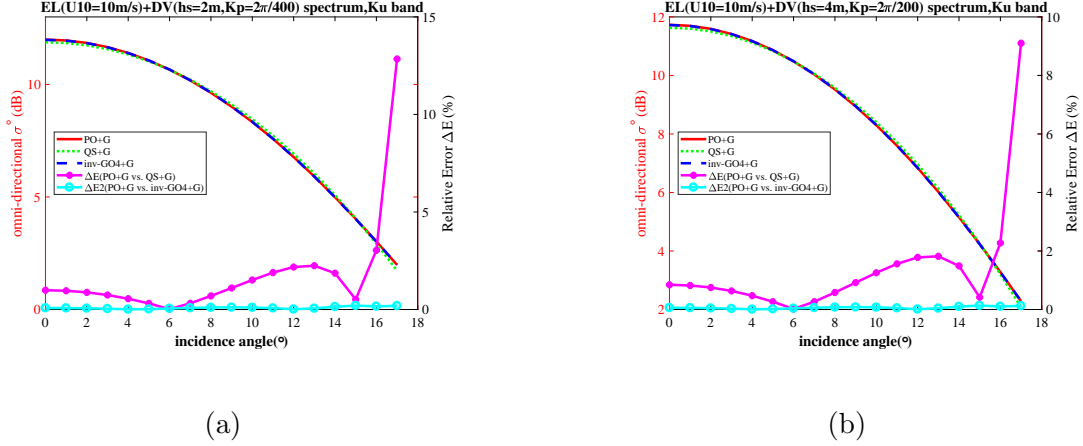


**Fig. 2.** Same as in Fig.1 but for mixed sea conditions: (a) El spectrum with  $U10=10$  m/s combined with swell spectrum with  $H_s=2$  m,  $K_p=2\pi/400$ . (b) El spectrum with  $U10=10$  m/s combined with swell spectrum with  $H_s=4$  m,  $K_p=2\pi/200$ .

(1982)). Fig. 1 and Fig. 2 present  $\sigma^0(\theta)$  calculated with PO for Ku-band and considering  
the anisotropic Gaussian case for the surface description. In Fig.1 surface conditions cor-  
respond to a pure wind sea case with a 10 m/s wind speed and a wave spectrum given by  
Elfouhaily et al. (1997)-named here after EL. In Fig.2, swell is taken into account in addi-  
tion, to represent mixed sea conditions. Here, the swell spectrum is defined as proposed by  
Durden and Vesecky (1985).

$$\psi(k, \varphi) = F(k)G(\varphi)$$

$$F(k) = \frac{H_s^2}{32\pi\sigma_l^2} \exp\left[-\frac{1}{2}\left(\frac{k - k_{peak}}{\sigma_l}\right)^2\right], \quad G(\varphi) = \frac{\cos^{14}(\varphi - \varphi_0)}{\int \cos^{14}(\varphi - \varphi_0) d\varphi} \quad (10)$$

where  $H_s$  is the significant wave height of the swell,  $K_{peak}$  is the peak wave number of  
the swell,  $\sigma_l$  the spectral width (fixed as  $\sigma_l=0.006$  rad/m). For Fig.2(a), we chose  $H_s=2$  m,  
 $K_{peak}=2\pi/400$  rad/m, while for Fig.2(b),  $H_s=4$  m,  $K_{peak}=2\pi/200$  rad/m.

The  $\sigma^0(\theta)$  values plotted in Fig.1 and Fig.2 represent  $\sigma^0(\theta)$  obtained as averaged values  
of individual values  $\sigma^0(\theta, \varphi)$  calculated over all azimuths  $\varphi$ . The light blue curve represent  
the results obtained by fitting the GO4 shape of Eq.(2) to the PO model (in all azimuths  
and then averaging), denoted by inv-GO4. The blue curve represents  $\sigma^0(\theta)$  of QS calculated

237 by fitting QS of Eq.(4) to PO. All these curves scale with the left axis. The relative errors  
 238 between different methods (inversed GO4, inversed QS) and the PO model are also plotted  
 239 with the right axis scale as reference. We define the relative error between PO and other  
 240 models as:

$$241 \quad err(\theta) = \frac{1}{N} \sum_{i=1}^N \left| \frac{\sigma_{po}^0(\theta, \phi_i) - \sigma_{mod}^0(\theta, \phi_i)}{\sigma_{po}^0(\theta, \phi_i)} \right| \quad (11)$$

242 Where  $N$  represents the number of azimuth angles in 0-360° for the same incidence angle,  
 243  $\sigma^0(\theta, \varphi)$  is in dB units.

244 The results show that for the three surface conditions illustrated here, the relative error  
 245 between the fitted GO4  $\sigma^\circ(\theta)$  and the PO values stay close to zero over the incidence range  
 246 of 0-17° (and a wind of 10 m/s). The errors for the QS inversion are larger than those for  
 247 inv-GO4 all over the 0-17° incidence range; for the incidence less than 15°, they stay of the  
 248 order of 1%, but increase rapidly with incidence, reaching more than 12% for incidence 17°. At 6° and 15°, the error approaches zero because the result of the fit of the QS model to the PO value (in dB) results in two crossing points of the curves close to these incidences.  
 249 In contrast the error of inversion with GO4 (inv-GO4) stays under 0.19% for all incidence  
 250 angles shown. Fig.2 also shows that taking into account swell in addition to wind sea (for a  
 251 wind of 10 m/s) does not change significantly the shape nor amplitude of  $\sigma^\circ(\theta)$ , compared  
 252 to the pure wind sea case (Fig.1). For the same wind speed, when a swell with a 2 m  
 253 significant wave height is added in the simulation (Fig.2a), the errors of the inv-GO4 model  
 254 and inverted QS model with respect to PO are almost not changed. But the addition of a  
 255 swell with a larger significant wave height (4 m in Fig.2b), makes the error of the QS model  
 256 reduce to about 9%, and that of inv-GO4 to 0.12% at the incidence of 17°. For both cases of  
 257 mixed sea condition, the inversion with GO4 provides values much closer to PO than does  
 258 the inversion with QS.  
 259  
 260

261 Using the GO4 model to fit  $\sigma_o$  values simulated with the PO model under anisotropic  
 262 Gaussian assumptions for the sea surface, we hence show that in Ku-band GO4 can reproduce  
 263 PO with the accuracy as high as the order of 0.2% for all incidence angles below 15°. This

264 high accuracy makes it possible to invert the high order statistics of the quasi-Gaussian sea  
 265 surfaces from the  $\sigma^0(\theta, \varphi)$  profiles measured by Ku-band radar with low incidences as it will  
 266 be shown in Section 4.

267 In appendix, the same type of analysis is presented for other radar wavelengths (in C  
 268 and Ka-band). It is found that with increasing radar frequency (from about 5 to 14 GHz)  
 269 the performance of the QS model respect to PO, increases whereas the performance of GO4  
 270 does not change significantly. This is because for QS model only the filtering effect is taken  
 271 into account, whereas for GO4 model both curvature and filtering effects are taken into  
 272 account. When the electromagnetic frequency is not very high, such as in C-band, ignoring  
 273 the curvature effect leads to a decreased accuracy of the QS model, whereas the GO4 model  
 274 which accounts for curvature effects keeps a good accuracy. When the electromagnetic  
 275 frequency increases, the conditions are closer to the optical limit and the curvature effect  
 276 are weaker for the short scales. So, with increasing frequency the accuracy of QS gets better  
 277 whereas that of GO4 stays almost constant.

278 Before using GO4 for inversion, it is necessary to define the interval of validity in terms of  
 279 radar geometry and surface conditions. As mentioned in Section 1, the final goal in our study  
 280 is to invert quasi-Gaussian slope statistical parameters for sea surfaces, especially the higher  
 281 order statistics, such skewness and peakedness coefficients. Because high order statistics  
 282 have a weak effect on the backscattering coefficients, an EM model with a high accuracy  
 283 is required to invert these statistics in order to avoid that the error of the EM model itself  
 284 contaminates the inversion. Therefore, we consider that the EM model is relevant only when  
 285 its error is small, *e.g.*, below 0.2% with respect to PO.

286 The relative error between GO4 is defined as  $\Delta E = \frac{1}{NM} \sum_{i=1}^N \sum_{j=1}^M \frac{|\sigma_{GO4}^0(\theta_i, \varphi_j) - \sigma_{PO}^0(\theta_i, \varphi_j)|}{|\sigma_{PO}^0(\theta_i, \varphi_j)|}$ .  
 287 Where  $N$  and  $M$  are the number of incidence and azimuth angles considered in the inversion.  
 288  $\sigma^0(\theta, \varphi)$  is in dB units. Table 1 shows the relative error ( $\Delta E(\%)$ ) between GO4 inverted  $\sigma^0$   
 289 and PO values in the case of pure wind sea (EL spectrum) for different incident ranges and  
 290 for different wind speed 2-18 m/s.

291 From Table 1, it is seen that a larger range of incidence range leads to larger errors. This

Table 1: the relative error ( $\Delta E(\%)$ ) between inv-GO4 and PO

wind speed(m/s)	2	4	6	8	10	12	14	16	18
$\Delta E(0-12^\circ)$	0.17847	0.00451	0.00168	0.00667	0.04478	0.06859	0.07658	0.07829	0.07730
$\Delta E(0-13^\circ)$	0.21292	0.00447	0.00545	0.00852	0.05275	0.09238	0.10654	0.11016	0.10929
$\Delta E(0-14^\circ)$	0.30127	0.01184	0.01494	0.01014	0.06046	0.11855	0.14260	0.14967	0.14948
$\Delta E(0-15^\circ)$	0.95597	0.05047	0.03868	0.00997	0.06409	0.14735	0.18414	0.19748	0.19910
$\Delta E(0-16^\circ)$	2.31700	0.36057	0.12206	0.01285	0.06763	0.17732	0.23681	0.25810	0.26176
$\Delta E(0-17^\circ)$	4.21928	0.55997	0.36373	0.04344	0.08787	0.20484	0.29885	0.33748	0.34734
$\Delta E(0-18^\circ)$	6.54778	1.26956	0.56968	0.26304	0.11783	0.22935	0.36916	0.43413	0.45499

292 increased errors is linked to the basic approximation of the GO4 formulation (Boisot et al.  
 293 (2015)) to approximate the PO model. Indeed this approximation is less and less valid when  
 294 the Rayleigh parameter increases, and this latter decreases with incidence as it involves the  
 295 electromagnetic wavenumber projected on the vertical axis.

296 One can choose the incidence range and wind speed range for the inversion by GO4  
 297 by setting a threshold on the inversion error. Here the accuracy threshold is set as 0.2%.  
 298 Table.1 shows that for wind speed from 4 to 18 m/s, and incidence ranges of 0-12° to 0-15°,  
 299 the relative errors  $\Delta E$  remain smaller than 0.2%. For very low wind speed (2 m/s) and larger  
 300 incidence range (0-16°, 0-17°, 0-18°),  $\Delta E$  are beyond 0.2%. From these simulation results, it  
 301 appears that for inversion with GO4, data should be limited to wind speeds within the 4-18  
 302 m/s range and incidence angle below 15°.

303 We have also calculated the errors between inv-GO4 values and PO values in the case of  
 304 a surface described by a mixed wave spectrum (EL+DV), and reached the same conclusion.

305 The next step for analyzing the conditions of applications of the GO4 is to assess the  
 306 domain of wavelength representative of the inverted parameters. In the following, without  
 307 losing the general properties of the GO4 model, we consider that slope and curvature param-  
 308 eters as well as the  $R$  parameter may be filtered parameters -also named effective parameters-  
 309 and by using our simulation cases, we examine to which extent this is true.

310 In the isotropic Gaussian case (Eq.1) these effective parameters are noted  $R_e$ ,  $mss_e$  and

311  $msc_e$ , respectively and  $mss_e$  and  $msc_e$  are defined from the wave number spectrum as:

$$\begin{aligned}
 312 \quad mss_e &= \int_0^{kd} k^2 \psi(\vec{k}) d\vec{k} \\
 msc_e &= \int_0^{kd} k^4 \psi(\vec{k}) d\vec{k}
 \end{aligned} \tag{12}$$

313 where the integral are truncated to an upper limit of wavenumber  $kd$  in [Hauser et al.](#)  
 314 [\(2008\)](#); [Thompson et al. \(2005\)](#). For the anisotropic and non-Gaussian case (Eq.2) the fil-  
 315 tered quantities are:

$$\begin{aligned}
 mssx_e &= \int_0^{kd} k_x^2 \psi(\vec{k}) d\vec{k}, \quad mssy_e = \int_0^{kd} k_y^2 \psi(\vec{k}) d\vec{k} \\
 mscx_e &= \int_0^{kd} k_x^4 \psi(\vec{k}) d\vec{k}, \quad mscy_e = \int_0^{kd} k_y^4 \psi(\vec{k}) d\vec{k} \\
 316 \quad mscxy_e &= \int_0^{kd} k_x^2 k_y^2 \psi(\vec{k}) d\vec{k} \\
 mss_e &= \int_0^{kd} k^2 \psi(\vec{k}) d\vec{k} = mssx_e + mssy_e \\
 msc_e &= \int_0^{kd} k^4 \psi(\vec{k}) d\vec{k} = mscx_e + mscy_e + 2mscxy_e
 \end{aligned} \tag{13}$$

317 In order to estimate the limit wave number value  $kd$  corresponding to the inverted mean  
 318 square slope and curvature parameters, we performed a series of inversion of the GO4 model  
 319 by fitting GO4 to  $\sigma^\circ(\theta, \varphi)$  values generated with the PO model. Inversion were applied over  
 320  $\sigma^\circ$  profile limited to the incidence range of  $[0-15^\circ]$ , for wind speeds between 4 and 16 m/s.  
 321 The outputs of the fitting process are the slope and curvature parameters of as well as the  
 322  $R$  coefficient. The method of inversion is non-linear least-square minimization algorithm (as  
 323 further used for real data inversion, see section 3).

324 The results for the isotropic case are plotted in [Fig.3](#). The results for the anisotropic case  
 325 are plotted in [Fig.4](#) and [Fig.5](#). In each case, the parameters inverted by fitting [Eq.\(1\)](#) or  
 326 [Eq.\(2\)](#) to simulated PO values at C-band (cyan), Ku-band (green) and Ka-band (magenta)  
 327 are compared on the same figures with the mean square slope and curvature calculated with  
 328 [\(Eq.12\)](#) and the EL spectrum truncated at a value of  $kd$  chosen such that the difference  
 329 between the two curves (from inversion and from [Eq.12](#)) is minimum. We found that this



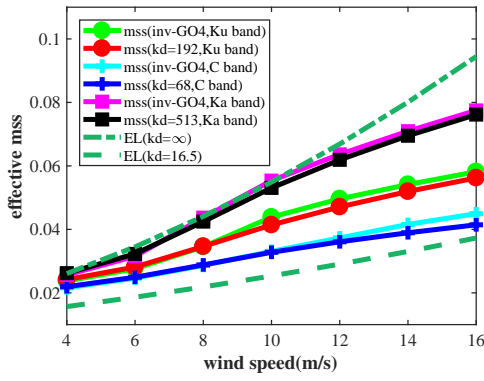
330 corresponds to  $kd=68$  rad/m (blue line),  $kd=192$  rad/m (red),  $kd=513$  rad/m (black), for  
 331 C, Ku and Ka-band respectively. In the same figure the slope or curvature variances for  
 332 the EL spectrum with  $kd=\infty$  (green dashed-dotted line) and  $kd=16.5$  rad/m (green dashed  
 333 line) are also shown. These latter curves correspond approximately to the cases of Cox and  
 334 Munk clean and slick sea surfaces, respectively in Wu (1972).

335 Fig.3(a) indicates that the  $mss$  obtained by fitting GO4 to PO, exhibit values interme-  
 336 diate between the CM slope variances of clean and slick sea surfaces. The inverted  $mss$   
 337 increases when the frequency increases. This shows that the inversion provides filtered  $mss$ .  
 338 Indeed the clean sea case of CM in Cox and Munk (1956, 1954), corresponds to  $kd=\infty$   
 339 since light scattering is sensitive to waves of all scales, whereas the slick case corresponds  
 340 to  $kd=16.5$  rad/m (minimum wavelength of about 38 cm) in Wu (1972). For Ku-band, the  
 341 wave length is about 2.2 cm, thus,  $kd$  is in the middle of the values corresponding to Cox  
 342 and Munk clean and slick sea cases.

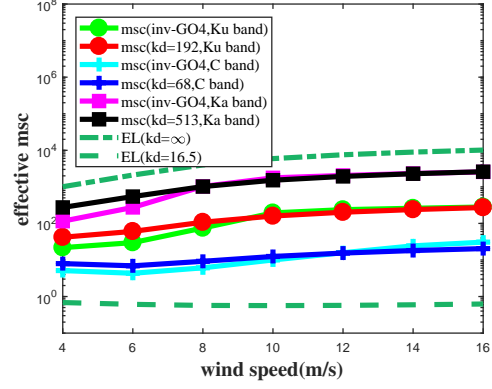
343 Fig.3(a) and (b) show that the omnidirectional curvature variances  $msc$  inverted from  
 344 GO4 have almost the same cutoff wave numbers as those for omnidirectional slope variances:  
 345  $kd$  192 rad/m for Ku-band, 68 rad/m for C-band and 513 rad/m for Ka-band. The order  
 346 of  $msc$  magnitude is smaller than that of Boisot et al. (2015). It is because filtered  $mss$  as  
 347 taken into account in our GO4 compensates the curvature effects in the model whereas  $mss$   
 348 in Boisot et al. (2015) are considered as total.

349 The results for non-isotropic case are shown in Fig.4 and Fig.5. The directional slope  
 350 variances  $mss_x$ ,  $mss_y$ , and curvature variances  $msc_x$ ,  $msc_y$ ,  $msc_{xy}$  have also almost the same  
 351 cutoff wave numbers as those for omnidirectional slope variances. Thus, we can confirm  
 352 that all the inverted slope and curvature variances GO4 are filtered, and have a unified  
 353 cutoff wave number for all parameters at a given frequency. For our inversion conditions  
 354 (incidence range 0-15°), the cutoff wavelength is 1.65, 1.48 and 1.41 times the wavelength of  
 355 the electromagnetic wave, at C, Ku and Ka-band, respectively.

356 We also examined the effect of the incidence angle on this estimation of the cutoff  
 357 wavenumber/wavelength. When varying the range of incidence used in the inversion from

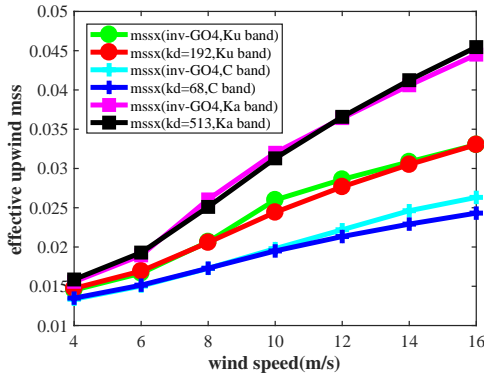


(a)

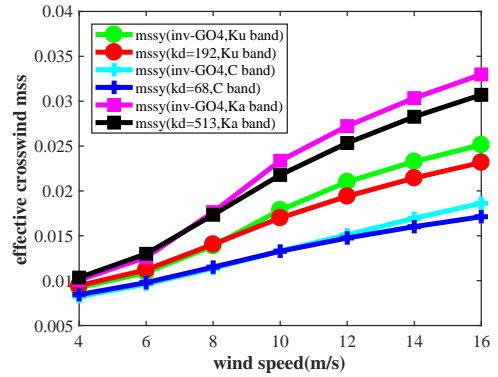


(b)

**Fig. 3.** Slope variances  $mss$  (Fig.3a) and curvature variances  $msc$  (Fig.3b) inverted using GO4 shape model fitted on PO simulated values of  $\sigma^0(\theta)$  over the incidence range  $[0-15^\circ]$  in the isotropic case. The PO values were simulated using the EL spectrum and wind speeds from 4 to 16 m/s. Results of inversion are shown for C-band (cyan), Ku-band (green) and Ka-band (magenta).  $Mss$  calculated with Eq. (12) with  $kd=68$  rad/m,  $kd=192$  rad/m,  $kd=513$  rad/m are shown in blue, red and black respectively.  $Mss$  values for  $kd = \infty$  (optical limit on clean sea) and  $kd=16.5$  rad/m (slick sea case of Cox and Munk) are shown with the dashed dotted and dashed green lines, respectively

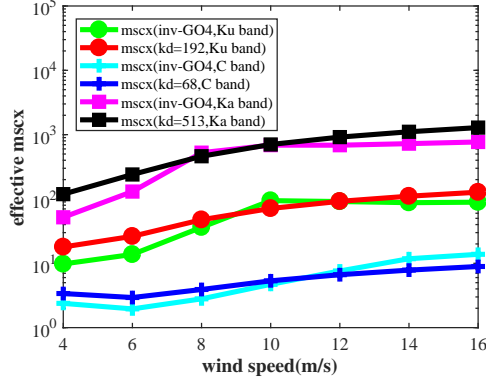


(a)

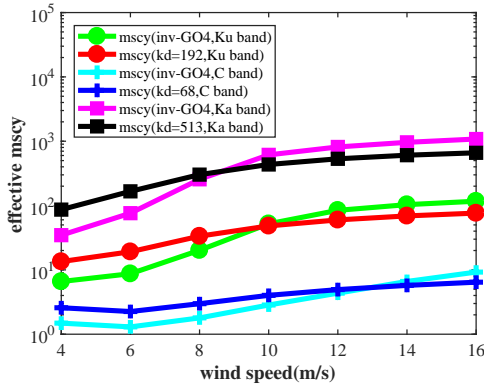


(b).

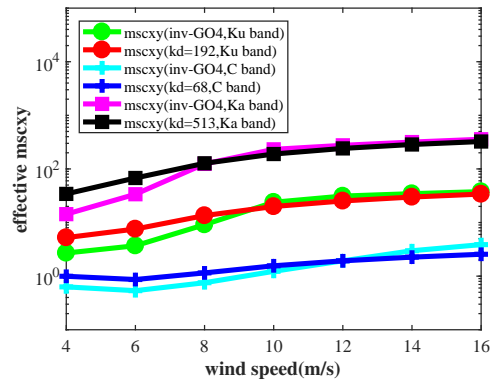
**Fig. 4.** Upwind (a) and Crosswind (b) slope variances inverted using GO4 shape model fitted on PO simulated values of  $\sigma^0(\theta, \varphi)$  over the incidence range  $[0-15^\circ]$ . The PO values were simulated using the EL spectrum and wind speeds from 4 to 16 m/s. Color codes and symbols are the same as in Fig.3.



(a)



(b)



(c)

**Fig. 5.** As in Fig.4, but for the mean square curvatures  $mscx$ ,  $mscy$  and  $mscxy$

358  $0-12^\circ$  to  $0-18^\circ$ , in the Ku-band case,  $kd$  increases from 174 rad/m to 210 rad/m; the cor-  
 359 responding cutoff wavelength value changes from 1.66 to 1.36 times the wavenumber of the  
 360 electromagnetic wave.

361 Fig. 6 shows the 8<sup>th</sup> parameter inverted in our approach, namely the effective reflection  
 362 coefficient  $R_e$ . For the three frequencies,  $R_e$  inverted are smaller than the values of  $R$ , the  
 363 theoretical Fresnel Reflection calculated at normal incidence from Klein and Swift (1977) at  
 364 the temperature of  $10^\circ\text{C}$  with a salinity of 0.35%.

365 This means that the inverted parameter  $R$  is indeed a kind of diffraction-modified Fresnel  
 366 coefficient due to the diffraction by waves of very small scales over a surface patch which  
 367 induces a reflection that is smaller than that by a plane. It is also found that for 4-16

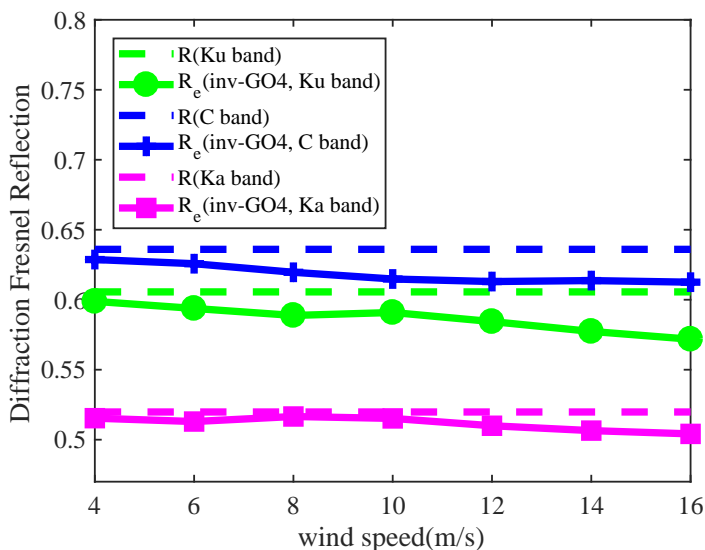


**Fig. 6.** Inverted Fresnel coefficient. Solid curves are for inverted values, dashed lines are for the theoretical Fresnel coefficient. Color code is: C-band in magenta, Ku-band in green, Ka-band in blue.

368 m/s this diffraction effect increases with wind speed. Such a trend agrees with the results  
 369 shown in Fig.6 in Freilich and Vanhoff (2003). It is noted however that our retrieved values  
 370 of  $R$  from GO4 at Ku-band are larger than those presented in Freilich and Vanhoff (2003)  
 371 which are derived by using the QS assumption. This indicates that  $R_e$  in GO4 includes less  
 372 diffraction effects than QS, because curvature effects are taken into account in the model.

373 In summary, we have shown with results of simulations presented in Fig.3 to 6, that all  
 374 the parameters obtained by inversion of GO4 are filtered quantities. In other words, only  
 375 the sea waves whose wavelength are greater than a certain threshold (cutoff wavelength)  
 376 contribute to the backscattering coefficient represented by the GO4 model.

### 377 3. Data

378 To invert sea slope PDF, we use HH-polarized  $\sigma^\circ$  data from the Precipitation Radar (PR)  
 379 of the TRMM satellite mission (Center (2001)).

380 PR on board the TRMM satellite is a microwave radar which provides the backscattering  
 381 coefficients at near-nadir incidence angles (0 to 18° from nadir). The PR antenna is an active

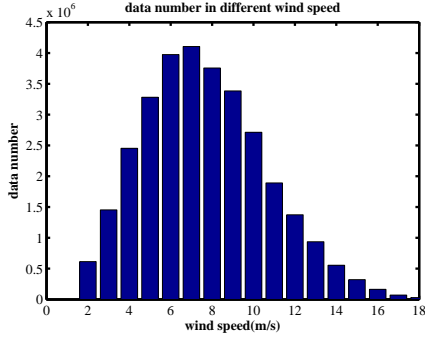
382 phased array system of 128 units. Each line consists of 49 pixel angles, and covers ground  
383 incidence angle in the across-track direction from  $-18^\circ$  to  $18^\circ$  with respect to nadir. Each  
384 scan line of PR lasts 0.6 seconds, and the data are obtained with a resolution of  $0.1^\circ$  in  
385 incidence. The backscattering coefficient (NCRS) data of PR are provided after a strict  
386 internal and external calibration. The data product used in this paper is PR standard  
387 product 2A21 (version-6) from the Distributed Active Archive Center. Nine years of data  
388 (2001-2009) of PR surface normalized radar cross-section have been selected over sea under  
389 no-rain conditions.

390 It is known that the inversion of the 2-D slope PDF needs 2-D backscattering coefficients.  
391 However, PR only provides 1-D backscattering with incident angles scanned across-track.  
392 Here, it is assumed that the parameters of the slope PDF are only related to the wind speed  
393 (as it is assumed in [Br on and Henriot \(2006\)](#); [Chu et al. \(2012a\)](#)), so that the normalized  
394 radar cross-section corresponding to a same wind speed at different space or time, can be  
395 combined to construct data sets of normalized radar cross-section versus two variables (in-  
396 cidence and direction with respect to the wind direction).

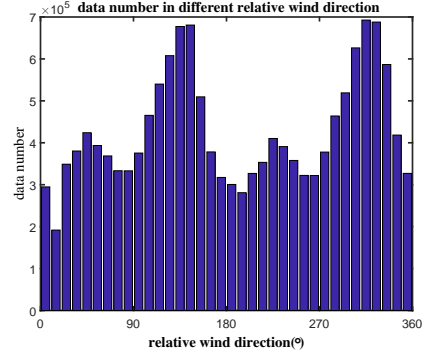
397 The wind data are provided by the buoy measurements of the National Data Buoy Cen-  
398 ter (NDBC) from NOAA. They are located in the Atlantic, Pacific, Gulf of Mexico and  
399 Caribbean Sea (same data set as used by [Chu et al. \(2012a\)](#)). The different NDBC buoys  
400 measure the wind speed at different heights. Here, all buoy wind speeds were normalized to  
401 an equivalent anemometer height of 10 m with the same parameters set as used in [Chu et al.](#)  
402 [\(2012a\)](#).

403 We re-use here the same co-located dataset as [Chu et al. \(2012a\)](#), where 82666 match-  
404 ing units are obtained (co-location criterium is a 50 km diameter area). This corresponds  
405 to 15774898 co-located pairs of wind and radar cross-section values. Please refer to the  
406 Appendix I in [Chu et al. \(2012b\)](#) for the construction of the collocated dataset in detail.

407 The co-located data are sorted by wind speed. Because the accuracy of wind speed is 2  
408 m/s, we have binned the NCRS data at the middle of the wind speed interval (for example  
409 9 m/s for all wind speeds from 8 m/s to 10 m/s). [Fig.7\(a\)](#) shows the number of data for



(a) Data number under different wind speed



(b) Data number under different relative wind direction.

**Fig. 7.** Matching data number under different wind speed and different relative wind direction.

410 different wind speeds, and Fig.7(b) shows the number of data for different relative wind  
 411 direction. The data are mainly distributed over wind speeds from 2 to 16 m/s. Based on  
 412 the results presented in section 2, we have limited our analysis to the wind speed range of 4  
 413 to 16 m/s.

414 To investigate the impact of sea states on quasi-Gaussian PDF slope, we distinguish two  
 415 categories of sea states. Using the criteria presented in (A1) of [Chu et al. \(2012a\)](#), we sorted  
 416 the ocean waves into pure wind sea and dominant swell cases (which can be mixed sea cases).

#### 417 4. Inversion Method

418 Before discussing the inversion method, the incidence range for the inversion has to be  
 419 examined again. In section 2, the limit on the incidence range was discussed from the accuracy  
 420 of GO4 model inversion compared to the PO model. Table 1 shows that this accuracy remains  
 421 lower than 0.2% for incidence ranges up to 15° for wind speeds larger than 4 m/s. Apart from  
 422 the accuracy of GO4, the sensitivity of the backscattering to the quasi-Gaussian slope PDF  
 423 parameters also need to be considered for the choice of the incidence angle range. Direct  
 424 modeling of  $\sigma^\circ$  as proposed in [Ping Chen and Huang \(2015\)](#) for the QS case, shows that a  
 425 variation in peakedness will more significantly affect medium incidence angles than incidence  
 426 angles very close to nadir. Thus, in order to efficiently invert the peakedness coefficients from

427 the  $\sigma^\circ$  profile, the largest possible range of incidence angle should be chosen. Based on the  
 428 two above constraints, the range of the incidence 0-15° is chosen as an appropriate trade-off  
 429 for the inversion by GO4.

430 In the anisotropic and quasi-Gaussian case, for a given wind speed, the normalized radar  
 431 cross-section is dependent on eleven parameters (Eq. (8)) among which seven parameters  
 432 describe the surface slope PDF ( $mssx_e$ ,  $mssy_e$ ,  $\lambda_{12}$ ,  $\lambda_{30}$ ,  $\lambda_{22}$ ,  $\lambda_{40}$ ,  $\lambda_{04}$ ), three parameters  
 433 are related to curvature variances ( $mscx_e$ ,  $mscy_e$ ,  $mscopy_e$ ) and the latter is the diffraction-  
 434 modified reflection coefficient  $R_e$ . In order to estimate the slope PDF parameters in the  
 435 anisotropic case, a method based on the 2-D backscattering coefficients (*i.e.*, described as a  
 436 function of incidence and azimuth angles) is required.

437 For convenience, we transform Eq.(8) into the following form:

$$\begin{aligned}
 \sigma_{GO4}^0(\theta, \varphi) = & \frac{|R_e|^2}{2\sqrt{mssx_e}\sqrt{mssy_e}} \sec^4(\theta) \exp\left(-\frac{1}{2}(X^2 + Y^2)\right) \times \\
 & \left\{ 1 + \begin{bmatrix} \frac{1}{4}\lambda'_{22}H_2(X)H_2(Y) \\ +\frac{1}{24}\lambda'_{40}H_4(X) \\ +\frac{1}{24}\lambda'_{04}H_4(Y) \end{bmatrix} \right. \\
 & \left. + \frac{1}{6} [3\lambda_{12}H_1(X)H_2(Y) + \lambda_{30}H_3(X)] \right\} \quad (14)
 \end{aligned}$$

439 Where

$$\begin{aligned}
 \lambda'_{22} = & \frac{mscopy_e}{Q_z^2 mssx_e \cdot mssy_e} + \lambda_{22}, \lambda'_{40} = \frac{m scx_e}{Q_z^2 mssx_e^2} + \lambda_{40} \\
 \lambda'_{04} = & \frac{mscy_e}{Q_z^2 mssy_e^2} + \lambda_{04}
 \end{aligned} \quad (15)$$

441 It is found that the form of Eq.14 for GO4 is the same as Eq.9 for QS for a quasi-Gaussian  
 442 sea surface except that  $\lambda'_{22}$ ,  $\lambda'_{40}$  and  $\lambda'_{04}$  in Eq.9 are replaced by  $\lambda'_{22}$ ,  $\lambda'_{40}$ , and  $\lambda'_{04}$  in  
 443 Eq.14. The parameters  $\lambda'_{22}$ ,  $\lambda'_{40}$ , and  $\lambda'_{04}$  are the sum of two terms. For an example  $\lambda'_{22}$ ,  
 444 is the sum of  $\lambda_{22}$ , and of term related to the curvature (curvature term). So if one wants  
 445 to use QS model directly to invert  $\lambda_{22}$ , then the inverted  $\lambda_{22}$  is not the real peakedness  
 446 coefficient, but a coefficient contaminated by the curvature effect. This curvature term in  
 447 each expression of Eq.15 is a small correction which involves a ratio of large quantities ( $m scx_e$ ,  
 448  $mscy_e$  or  $mscopy_e$  and  $Q_z^2$ ), as well as small quantities  $mssx_e$ ,  $mssy_e$  in denominator. Taking

449  $mssx_e$ ,  $mssy_e$ ,  $mscx_e$ ,  $mscy_e$  and  $mscopy_e$  in the curvature term as parameters to be inverted  
450 simultaneously with the other parameters of Eq.14 is subject to large errors. Thus, instead of  
451 inverting those parameters in the curvature terms simultaneously with the PDF coefficients,  
452 we directly calculate the curvature terms with Eq.13 and the EL wind sea spectrum of the  
453 corresponding known wind speeds and  $kd$ . We checked that when using the  $mssx_e$ ,  $mssy_e$ ,  
454  $mscx_e$ ,  $mscy_e$  and  $mscopy_e$  values for the mixed wind sea and swell (EL/DV spectrum) case,  
455 the obtained curvature terms are very close to those of the wind sea case (EL spectrum),  
456 with difference smaller than 1%.

457 Then finally, the eight inverted parameters are  $R_e$ ,  $mssx_e$ ,  $mssy_e$ ,  $\lambda_{12}$ ,  $\lambda_{30}$ ,  $\lambda_{22}$ ,  $\lambda_{40}$   
458 and  $\lambda_{04}$  are obtained by fitting Eq.14 to the 2-D  $\sigma^0(\theta, \varphi)$  measurements over the chosen  
459 range of incidence angles 0-15.1° (PR incidence angle nearest to 15°) and over all azimuth  
460 angle 0-360°. The non-linear inversion is based on the minimization of the mean squared  
461 difference between the measured  $\sigma^0(\theta, \varphi)$  and GO4 model values expressed in dB where this  
462 cost function sums for each wind speed class, all the values over the incidence and azimuth  
463 angles. This non-linear least-square minimization requires initial values of  $R_e$ ,  $mssx_e$ ,  $mssy_e$   
464 that we set as the results obtained by fitting PR  $\sigma^0(\theta, \varphi)$  to QS model for a Gaussian sea  
465 surface (Eq.4), it also requires initial values for  $\lambda_{12}$ ,  $\lambda_{30}$ ,  $\lambda_{22}$ ,  $\lambda_{40}$  and  $\lambda_{04}$  that we set as the  
466 values proposed by Cox and Munk (1954). Finally, the seven parameters:  $mssx_e$ ,  $mssy_e$ ,  $\lambda_{12}$ ,  
467  $\lambda_{30}$ ,  $\lambda_{22}$ ,  $\lambda_{40}$  and  $\lambda_{04}$  of the slope PDF, are obtained.

468 Here, the non-linear least square inversion algorithm does not use the approximation of  
469  $\log(1+t) \approx t$  when  $t$  is a small quantity, which was the approximation used by Cox and Munk  
470 (1954, 1956). According to Cox and Munk (1954), this approximation causes inherent errors  
471 of the order of 10%. But in fact it is dependent of  $t$  which is a complex combination of  
472 several parameters. We could checked with numerical tests on PDF inversion with and  
473 without this approximation, for an example of a wind of 10 m/s, that the linearization of  
474 the PDF proposed by Cox and Munk may induce a bias of up to about 15% on  $\lambda_{12}$ , 25% on  
475  $\lambda_{22}$  and even more than 100% on  $\lambda_{40}$ . The error on the other parameters is less than 10%.

476 It is also noted that because  $R_e$  is one of our inverted parameters, any overall calibration



477 error in the radar measurement will be reflected in  $R_e$ , so that the PDF inverted parameters  
 478 depend only on the shape of  $\sigma^\circ(\theta, \varphi)$ , and not on the absolute values of  $\sigma^\circ(\theta, \varphi)$ . This means  
 479 that potential error on radar calibration will have no important effect on the PDF inversion.

## 480 5. Inversion Result

481 We co-located in time and space the PR data sets of nine years (2001-2009) with the  
 482 corresponding buoy measurements. Then, based on the data set, we inverted the seven  
 483 parameters of the quasi-Gaussian PDF using the GO4 model and method presented here  
 484 above.

485 To evaluate the inversion performance, the relative inversion error is defined as  $err =$   
 486  $\frac{1}{N \cdot M} \sum_{i=1}^N \sum_{j=1}^M \left| \frac{\sigma_{PR}^0(\theta_i, \varphi_j) - \sigma_{GO4}^0(\theta_i, \varphi_j)}{\sigma_{GO4}^0(\theta_i, \varphi_j)} \right|$  where  $\sigma^0(\theta_i, \varphi_j)$  is in dB units.

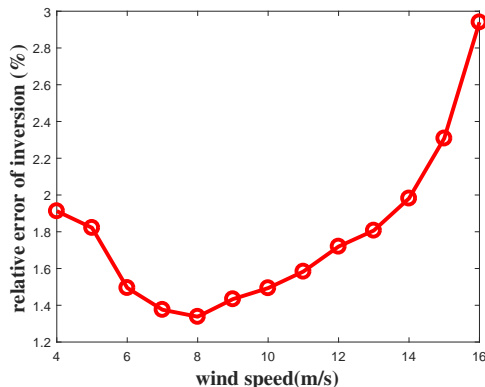


Fig. 8. Relative inversion error under different wind speeds.

487 Fig.8 shows the inversion error under different wind speeds. At low wind speeds, the  
 488 errors decreases with wind speed and reaches a minimum at a wind speed of 8 m/s; for wind  
 489 speeds larger than 8 m/s the error increases with wind speed. The inversion error trend with  
 490 wind speed is consistent with Table 1 (section 2) which shows the mean difference between  
 491 GO4 and PO model . In addition, larger errors at wind speeds of 13 to 16 m/s may also be  
 492 attributed to a smaller number data in these conditions, as shown in Fig.7(a).

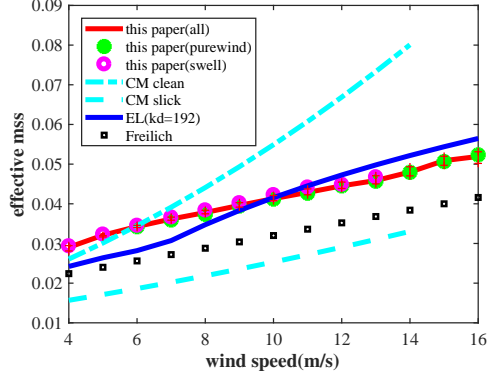
493 5.1. Second Order Statistical Properties-Slope Variance

494 Fig.9(a) shows the filtered (effective) omnidirectional  $mss_e$  as a function of wind speed,  
 495 obtained by fitting Eq.(14) to the PR  $\sigma^\circ(\theta, \varphi)$  data in the incidence angles of 0-15.1°, under  
 496 conditions of dominant swell (magenta open circles), pure wind wave (green circles) and  
 497 all cases (red line). Error bars around  $mss_e$  for all cases show the effect of changing by  
 498  $\pm 0.7$  degree the incidence angle interval considered in the inversion. The figure also shows  
 499 a comparison with the results of Cox and Munk (1956, 1954) for clean and slick sea surface  
 500 (dashed-dotted and dashed curves, respectively), the results obtained by Freilich and Vanhoff  
 501 (2003) (black open squares), and the results calculated with Eq.(13) and the EL spectrum  
 502 limited to  $kd=192$  rad/m (blue line). Fig.9(b)(c) show similarly the upwind  $mssx_e$  and  
 503 crosswind  $mssy_e$  as a function of wind speed.

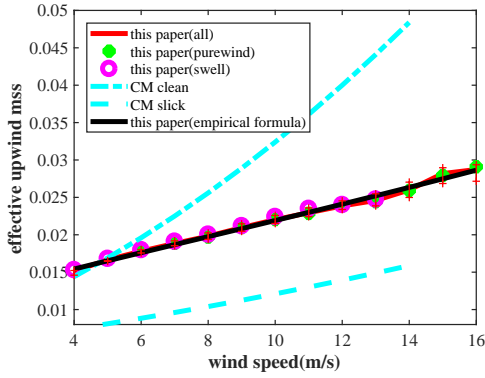
504 The general trend of the inverted  $mss$  with wind speed is similar to the logarithmic  
 505 relationship proposed by Wu (1972). It exhibits values and trend intermediate between the  
 506 CM slope variances of clean and slick sea surfaces. As shown above, the cutoff wavenumber  $kd$   
 507 corresponding to the PR analysis is also about 192 rad/m, which is similar to the simulation  
 508 result discussed in section 2. Fig.9(a) also shows that the slope variances  $mss_e$  are larger than  
 509 those of Freilich and Vanhoff (2003) by about 20%-30%. This is because the slope variances  
 510 of Freilich and Vanhoff are inverted using the QS model and Gaussian slope PDF, and their  
 511 results correspond to  $kd=50-70$  rad/m by Chu (2011); Freilich and Vanhoff (2003).

512 From Fig.9, it is shown that adding swell mainly affects the crosswind  $mss$  which are  
 513 slightly higher in swell conditions (Fig.9c). Although not visible in the figures, we confirmed  
 514 however that  $mss$ ,  $mssx$  and  $mssy$  for mixed cases with wind sea and swell are larger than  
 515 those for pure wind sea. All these results on the effect of the sea conditions on slope variances  
 516 are consistent with those obtained by Chu et al. (2012a)

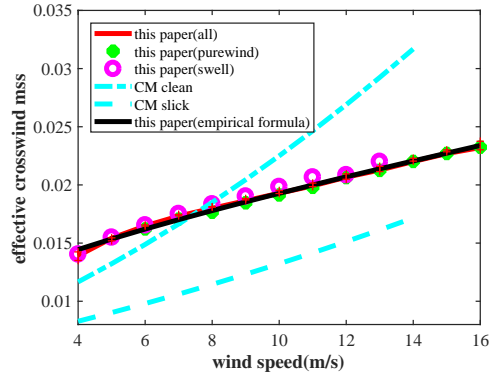
517 We also compared the slope variances in crosswind and upwind obtained with our ap-  
 518 proach with those obtained by Chu et al. (2012a) and found that ours are both larger by  
 519 about 20%-30% than theirs (not shown). When adding the slope variances in crosswind and  
 520 upwind of Chu et al. (2012a), we re-produce their total slope variances and find that they



(a) Effective omnidirectional  $mss$



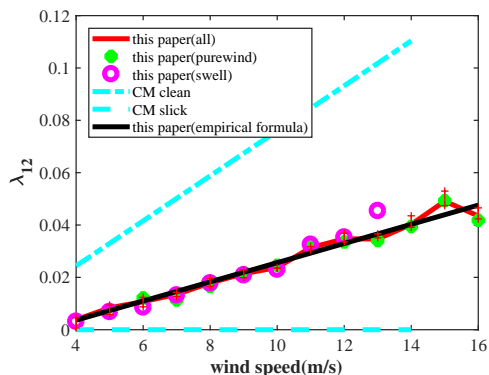
(b) Effective  $mss$ (upwind)



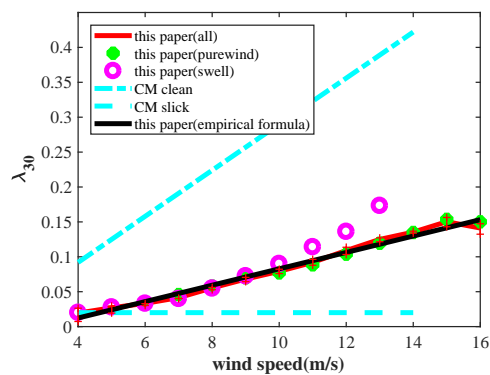
(c) Effective  $mss$ (crosswind).

**Fig. 9.** Inverted slope variance: effective omnidirectional  $mss$  (a), effective upwind  $mss$ (b) and effective crosswind  $mss$  (c) as function of wind speed. Magenta open circles, green dots and red curve represent the results inverted by fitting GO4 to PR data under conditions of dominant swell, pure wind waves and all cases with incidence angle range  $0-15.1^\circ$ , respectively. Error bars show the effect of changing by  $\pm 0.7^\circ$  the incidence angle interval considered in the inversion (only visible at the highest wind speeds). In (a), black open squares represent the results obtained by Freilich and Vanhoff (2003). Dashed-dotted and dashed curves correspond to the results of Cox and Munk for clean and slick sea. Cyan lines represents the results calculated with Eq.(13) and the EL spectrum truncated at  $kd=192$  rad/m. In (b) and (c), the results calculated with the empirical formula Eq.(16-a) and (16-b) are also plotted by black thick lines.

521 are very close to those of Freilich and Vanhoff (2003).



(a) Relationship of skewness coefficient  $\lambda_{12}$  with wind speed



(b) Relationship of skewness coefficient  $\lambda_{30}$  with wind speed.

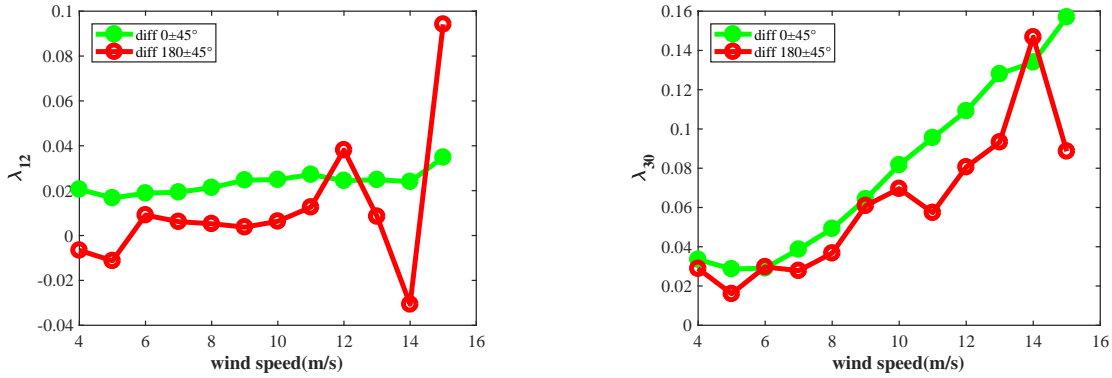
**Fig. 10.** Inverted skewness coefficients as functions of wind speed for (a)  $\lambda_{12}$  (b)  $\lambda_{30}$ . Color codes and symbols are similar to Fig.9.

523 Fig.10(a),(b) show skewness coefficients  $\lambda_{12}$  and  $\lambda_{30}$  as a function of wind speed obtained  
 524 from inversion of the PR data by fitting GO4. Color codes and symbols are the same as  
 525 in Fig.9(b). It can be observed that skewness  $\lambda_{12}$  and  $\lambda_{30}$  inverted from PR data exhibit  
 526 values intermediate between those of CM for the two cases (clean and slick sea). This may  
 527 be attributed to the fact that skewness coefficients are dominated by the shortest waves.  
 528 Indeed, with a cutoff limit of the GO4 model of about 3.2 cm (see section 2), the retrieved  
 529 skewness coefficients are lower than those of all scale waves observed by CM for clean sea,  
 530 and higher than those of the waves with the cutoff wavelength of 38 cm observed by CM for  
 531 slick sea surfaces in Wu (1972).

532 Fig.10 also shows that skewness coefficients  $\lambda_{12}$  and  $\lambda_{30}$  increase with wind speed. This  
 533 tendency agrees with CM results for a clean sea, with the results by Chu et al. (2012a) and  
 534 by Br on and Henriot (2006).  $\lambda_{12}$  and  $\lambda_{30}$  inverted by our method are a little bit larger than  
 535 Chu's values (not shown here). This may result from the difference in the numerical method  
 536 (Chu used the approximation  $\log(1+t) \approx t$ , which causes errors inherent to the numerical  
 537 inversion as discussed in section 4.)

538 Fig. 10(a-b) also shows that sea state conditions significantly affect the skewness coefficient  
 539 mainly at wind speeds above 10-11 m/s where both skewness coefficients are larger in  
 540 dominant swell conditions than in pure wind sea conditions.

541 This is consistent with the results of Chu et al. (2012a), who found that  $\lambda_{12}$  and  $\lambda_{30}$   
 542 under dominant swell are larger than those under pure wind waves.

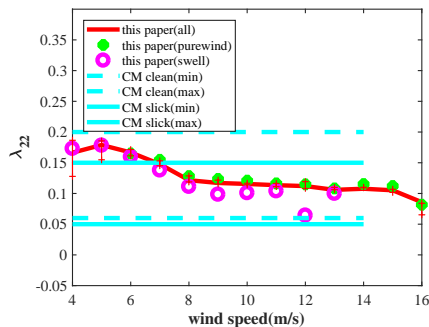


(a) Effect of wind vs. wave direction  
 on skewness coefficient  $\lambda_{12}$

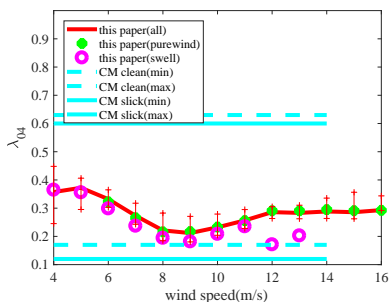
(b) Effect of wind vs. wave direction  
 on skewness coefficient  $\lambda_{30}$ .

**Fig. 11.** Effect of wind vs. wave direction on skewness coefficients (a) for  $\lambda_{12}$ , (b) for  $\lambda_{30}$ .

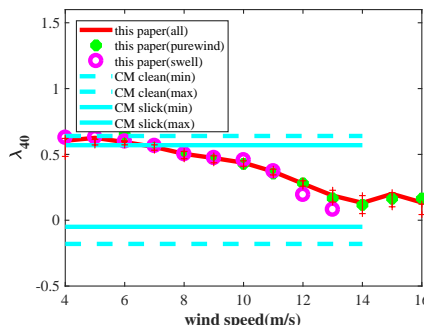
543 We also studied the effect of wind vs. wave direction on skewness coefficients. Fig.11  
 544 shows the skewness coefficients as a function of wind speed for two categories of angle between  
 545 wind and wave directions, the first one for waves more or less parallel to the wind ( $0^\circ \pm 45^\circ$ ,  
 546 green), the second for waves opposite to the wind ( $180^\circ \pm 45^\circ$ , red). From Fig.11(a-b) it is  
 547 found that for waves propagating along-wind and moderate winds (up to 11 m/s), both  $\lambda_{12}$   
 548 and  $\lambda_{30}$  are larger than in the case of opposite waves. At larger winds the number of data  
 549 sets with opposite waves is relatively small. Therefore, the inversion errors for these cases  
 550 are larger than 4%. So we can only conclude that for wind speed between 4 and 11 m/s,  
 551  $\lambda_{12}$  and  $\lambda_{30}$  are larger in cases of wind and waves aligned compared to cases where they are  
 552 opposite. This may be explained by the fact that waves whose direction is not aligned with  
 553 the wind direction will decrease the asymmetry of sea surface slope in upwind and downwind  
 554 directions.



(a) Relationship of peakedness coefficient  $\lambda_{22}$  with wind speed.



(b) Relationship of peakedness coefficient  $\lambda_{04}$  with wind speed.



(c) Relationship of peakedness coefficient  $\lambda_{40}$  with wind speed.

**Fig. 12.** Inverted peakedness coefficients as functions of wind speed.

556 Fig. 12(a)(b)(c) show the results for the peakedness coefficient  $\lambda_{22}$ ,  $\lambda_{04}$  and  $\lambda_{40}$  where  
 557 color codes and symbols are the same as in Fig. 9(b).

558 In Fig. 12, over the whole wind speed conditions, our values are within the limits found by  
 559 CM for each case (clean and slick sea). Thanks to our non-linear inversion (in opposite to the  
 560 case of CM) we are able to bring more details on the peakedness parameters. In particular,  
 561 we find that decreases  $\lambda_{40}$  with wind speed up to 14 m/s and then remains constant.  $\lambda_{22}$   
 562 and  $\lambda_{04}$  tend to decrease with wind speed up to a wind speed of 8 m/s and then remain  
 563 stable ( $\lambda_{22}$ ) or increase slightly ( $\lambda_{04}$ ). In opposite, Cox and Munk could only provide a large  
 564 range of possible values without possibility to identify significant difference between clean  
 565 and slick sea cases nor trends with wind speed.

566 Fig.12(a)(b) also show that the presence of the swell tends to induce smaller values of  
 567 the peakedness coefficients and at least for wind conditions larger than 6 m/s for  $\lambda_{22}$  and  
 568  $\lambda_{04}$  for largest than 11 m/s for  $\lambda_{40}$ .

569 So peakedness effect seem to be less sensitive to wind speed than skewness coefficients  
 570 (see above) and less sensitive to the presence of swell. Their tendency to decrease with wind  
 571 speed in light to moderate winds while staying more or less stable for higher winds may  
 572 be attributed to a smaller uniformity of the wave slope distribution along the long wave  
 573 profiles at light winds, according to the phenomenological model proposed by Chapron et al.  
 574 (2000). The same interpretation might be raised to explain the smaller values of peakedness  
 575 coefficients when swell is present.

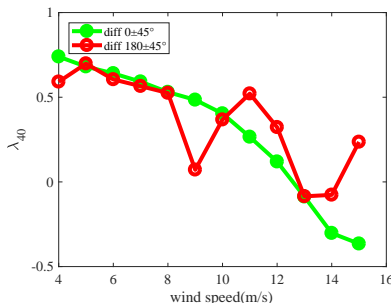


**Fig. 13.** Effect of wind vs. wave direction on peakedness coefficient  $\lambda_{40}$

576 We also studied the effect of wind vs. wave direction on peakedness coefficients. Fig.13  
 577 shows the peakedness coefficient  $\lambda_{40}$  as a function of wind speed for two categories of angle  
 578 between wind and wave directions (similar to the categories in Fig.10). In opposite to the  
 579 results on skewness shown here above, we find that the angle has no clear effect on  $\lambda_{40}$ . We  
 580 also analyzed the peakedness coefficients  $\lambda_{22}$  and  $\lambda_{04}$  with the same categories of wind/wave  
 581 angles (not shown here) and draw the same conclusion as for  $\lambda_{40}$ .

#### 582 5.4. Sensitivity to the choice of the angular domain

583 To assess our results we also studied the effect of the incidence range on the inversion of  
 584 the slope pdf parameters. For that purpose, 6 incidence ranges for PR data (0-12.8°, 0-13.5°,  
 585 0-14.3°, 0-15.1°, 0-15.9°, 0-16.5°) were tested for the inversion, one by one. We found that

586 the values of  $mss$ ,  $mssx$  and  $mssy$  increase with the incidence range; the increments are  
 587 within about 10% for the incidence range from 0-14.3° to 0-16.8°. This is because when  
 588 increasing the range of incidence angle, while remaining in quasi-specular conditions, the  
 589 radar backscatter is more sensitive to short scales waves, that correspond larger slopes.  
 590 With the incidence ranges increasing from 0-14.3° to 0-15.9°, the skewness coefficient  $\lambda_{30}$   
 591 increases by about 10% for the wind speeds larger than 8 m/s, while  $\lambda_{12}$  decreases with the  
 592 incidence range from 0-14.3° to 0-16.8° for the wind speed between 6 m/s to 15 m/s. For the  
 593 smaller incidence range, such as 0-12°, 0-12.8° the inverted peakedness coefficients  $\lambda_{22}$ ,  $\lambda_{40}$   
 594 and  $\lambda_{04}$  have a divergence. It may be due to the fact that for the small incidence range the  
 595 sensitivity of radar backscattering to the peakedness coefficients is weak (Chu (2011)). The  
 596 divergence reduces rapidly with increasing incidence range, and disappears starting from the  
 597 0-14.3° range. When varying the incidence range from 0-14.3° to 0-16.8°, the peakedness  
 598 coefficients change by about 10%. Overall the conclusions on the trend with wind speed,  
 599 presence of swell and relative wave directions do not change when varying the incidence  
 600 range from 0-14.3° to 0-16.8°.

### 601 5.5. Empirical Formulae

602 Based on the relationships of the seven parameters of quasi-Gaussian slope PDF with  
 603 wind speed from 4 m/s to 16 m/s, based on the inversion results for the incidence range 0-15°  
 604 (solid red curves) shown in Fig.8-11, we propose empirical formulae, for quasi-Gaussian sea  
 605 slope parameters corresponding to a cutoff limit of 192 rad/m (associated with Ku-band  
 606 observations from 0-15° incidence). In this process, we use some analytical shapes proposed  
 607 in past study, such as a logarithmic dependence with wind speed for the slope variances  
 608 (Hauser et al. (2008); Wu (1972)), and linear relationships for skewness coefficients with  
 609 wind speed as proposed by Cox and Munk (1956). In spite of the trend of the three peaked-  
 610 ness coefficients with wind speed shown in Fig.12, we still use the linear fit for peakedness



611 coefficients. We obtained the following empirical formulae:

$$612 \quad m_{ssx_e} = 0.009416 \times e^{(0.2188 \times U^{0.5868})} \pm 0.0041 \quad (16a)$$

$$613 \quad m_{ssy_e} = 0.007392 \times e^{(0.3895 \times U^{0.3911})} \pm 0.0027 \quad (16b)$$

$$614 \quad \lambda_{12} = 0.003663 \times U - 0.01101 \pm 0.0139 \quad (16c)$$

$$615 \quad \lambda_{30} = 0.01174 \times U - 0.03462 \pm 0.0443 \quad (16d)$$

$$616 \quad \lambda_{40} = -0.04646 \times U + 0.8565 \pm 0.1786 \quad (16e)$$

$$617 \quad \lambda_{22} = -0.006796 \times U + 0.1944 \pm 0.0276 \quad (16f)$$

$$618 \quad \lambda_{04} = -0.004321 \times U + 0.3273 \pm 0.0466 \quad (16g)$$

619

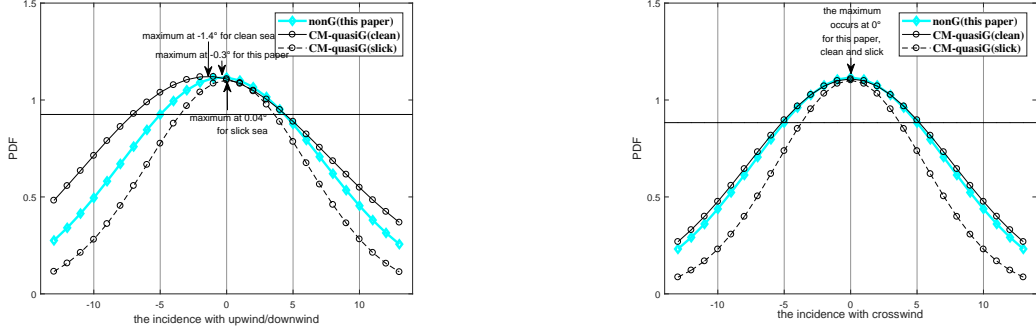
620

621 Note that the mean values of our inverted peakedness coefficients ( $\lambda_{22}=0.1265\pm0.0276$ ,  
622  $\lambda_{40}=0.3919\pm0.1786$  and  $\lambda_{04}=0.2841\pm0.0466$ ) agree well with those given by [Br on and Henriot](#)  
623 [\(2006\)](#) that were obtained from optical data; this indicates that the peakedness coefficients  
624 can be inverted correctly from Ku-band radar observations using the GO4 model.

### 625 5.6. Slope Probability Density Distribution

626 Using the above empirical formulae, valid for Ku-band radar data over the incidence  
627 range of 0-15 . the sea surface slope PDF can be obtained for different the wind speeds in  
628 the range 4-16 m/s.

629 Fig.14(a) shows the slope PDF  $p(\tan(\theta),0)$  or a wind speed of 10 m/s in upwind and  
630 downwind direction, obtained from the PR data inversion with the quasi-Gaussian PDF  
631 (blue curve), from CM for a clean sea (black solid curve with open circles) and from CM for  
632 a slick sea (black dotted curve with open circles). The horizontal axis is the slope angle  $\theta$ ,  
633 where the positive sign is for upwind direction. In the along-wind direction (Fig.14a), the  
634 PDF retrieved from our analysis is intermediate between the clean sea and the slick case  
635 of Cox and Munk, with higher probability of large slopes than in the slick case but lower  
636 probability of large slopes than in the clean case. This is mainly due to the filtering effects



(a)  $p(\tan(\theta),0)$  in upwind direction

(b)  $p(0,\tan(\theta))$  in crosswind direction

**Fig. 14.** Slope PDF in upwind (a) and crosswind (b) directions, under the condition of a 10 m/s wind speed. In (a) the arrows represent the maximum of the PDF (at  $-0.3^\circ$ ,  $-1.4^\circ$ ,  $0.04^\circ$  for PR data, CM clean sea and CM slick sea, respectively); in (b) the PDF maximum is at the same position ( $0^\circ$ ), for the three models.

637 because waves, which contribute to our analyzed signals are not shorter than 3.2 cm, as shown  
 638 above. The shape of the along-wind slope PDF is also slightly different because of skewness  
 639 and peakedness effects. In particular skewness is responsible of the shift of the maximum  
 640 of the curve with respect to the 0 slopes ( $-0.3^\circ$  for our results compared to  $-1.4^\circ$  and  $0.04^\circ$   
 641 for respectively the CM clean sea, and the CM slick sea cases). This is associated with  $\sigma^\circ$   
 642 values which are with slightly larger at the low incidence angles in downwind direction than  
 643 in upwind direction. We could confirm this feature by a direct inspection of  $\sigma^\circ$  variations  
 644 with azimuth.

645 Similarly, Fig.14b shows the slope PDF along the crosswind direction  $p(0,\tan(\theta))$ . The  
 646 PDF retrieved from our analysis is very close to that corresponding to the clean sea case of  
 647 Cox and Munk. This was already apparent in Fig.9c with crosswind  $mss$  values much closer  
 648 to the clean sea case than in the case of upwind  $mss$  (Fig.9b). The axis of symmetry of the  
 649 slope PDF is located in the incidence angle of  $0^\circ$  for all the three cases, *e.g.* there is no angle  
 650 deviation for the slope PDF along the crosswind direction. All these features indicate that in  
 651 the crosswind direction, the slope PDF derived from microwave measurements behave very  
 652 similarly to the optical case.

## 653 6. Conclusion

654 Up to now only analyses from optical data have provided information on the seven pa-  
655 rameters of the quasi-Gaussian wave slope PDF and their relation with wind speed. These  
656 results cannot be transposed directly in the application of ocean microwave remote sensing  
657 because of the diffraction effects at wavelengths longer than optical ones. In this paper,  
658 using a GO4 scattering model and TRMM/PR normalized radar cross-section, we estimate  
659 the seven parameters of the quasi-Gaussian wave slope PDF at Ku-band. This is done by  
660 applying a nonlinear fit of this model to the 2-D backscattering coefficients (as a function of  
661 incidence angle and azimuthal angle with respect to the wind).

662 In a first step, we checked from simulation performed under a Gaussian assumption and  
663 for Ku, C and Ka-bands that even if curvature effects are included in GO4, the approach  
664 provides filtered variances of slope and curvature, as well as an effective Fresnel coefficient.  
665 For a given electromagnetic frequency, the same cutoff was obtained for slope variances  
666 and curvature variances. This filtered effect decreases when the electromagnetic wavelength  
667 decreases. In our conditions this filtering effect was estimated to be at 3.2 cm, *e.g.* 1.45  
668 times the electromagnetic wavelength. The slope variances inverted by using the GO4 model  
669 are all larger than those inverted by using the Quasi-Specular model, because the curvature  
670 effect is taken into account in GO4, which makes more small scale waves being inverted by  
671 GO4 than by QS without curvature correction. We also assessed that the optimal range of  
672 incidence angles to be used in the inversion with the GO4 model is 0-15°.

673 Our results obtained by the TRMM/PR data set confirm that the inverted mean square  
674 slopes correspond to a filtered surface with filtering effects however less important than when  
675 the QS model is used for inversion.

676 The general trend of mean square slopes retrieved from this analysis is consistent with  
677 previous results also obtained in Ku-band (Hauser et al. (2008); Chu et al. (2012a)). One  
678 important point to note is that the crosswind  $mss$  are closer to the clean sea case of CM  
679 than are the alongwind  $mss$ .

680 Concerning the third order statistical properties, we find that skewness coefficients  $\lambda_{12}$

681 and  $\lambda_{30}$  lie between those of CM for the clean and slick sea conditions and clearly increase with  
682 wind speed as found for the optical case by [Cox and Munk \(1954, 1956\)](#); [Br on and Henriot](#)  
683 [\(2006\)](#). The existence of swell in addition to wind sea tends to increase the skewness co-  
684 efficients with respect to cases of pure wind sea, specially at the higher winds. The angle  
685 between wave direction and wind direction also affects the skewness coefficients. When waves  
686 propagate along the wind direction ( $\pm 45^\circ$ ) the skewness coefficients  $\lambda_{12}$  and  $\lambda_{30}$  are larger  
687 than when waves propagate in the opposite direction. These results are important because  
688 they may explain the trends and part of variability of the upwind to downwind ratio of the  
689 backscatter signals in remote sensing.

690 As for the peakedness coefficients  $\lambda_{22}$ ,  $\lambda_{40}$  and  $\lambda_{04}$  inverted by using GO4, they are within  
691 the intervals of values found Cox and Munk for all their analyzed sea conditions (clean sea  
692 or slick sea). Thanks to our non-linear inversion method without the linearization used by  
693 previous authors (Cox and Munk, Chu), the accuracy on the peakedness coefficient is higher  
694 so that we could evidence the dependence of the peakedness coefficients with wind speed and  
695 sea state conditions. Although they are less variable than the skewness coefficient with wind  
696 speed, their tendency may indicate a smaller uniformity of the wave slope distribution along  
697 the long wave profiles at light winds compared to moderate or high winds, according to the  
698 phenomenological model proposed by [Chapron et al. \(2000\)](#). The same interpretation might  
699 be raised to explain the smaller values of peakedness coefficients when swell is present.

700 In addition, empirical linear models are proposed in this paper for the seven retrieved  
701 parameters of the quasi-Gaussian slope PDF as a function of wind speed.

702 Overall, the slope PDF reconstructed from the microwave observations in Ku-band are  
703 either intermediate between those of the optical limit and the slick sea case of Cox and Munk  
704 (along wind direction) or very similar to that of the optical limit (crosswind direction).

705 It should be pointed out that for a given space-time point, the PR radar only provides  
706 the 1-D backscattering coefficient as a function of incidence angle cross-track. However,  
707 2-D backscattering coefficients are necessary for a 2-D slope inversion. Therefore in this  
708 paper, we have combined the backscatter coefficients corresponding to a same wind speed

709 at different space or time to construct 2-D backscattering coefficients for 2-D slope inversion  
710 at that wind speed. However, the combinations need the assumption that the slope PDF  
711 parameters are only related to the wind speed.

712 Other kind of radar working at low incidence, wave spectrometer (see *e.g.*, [Jackson et al.](#)  
713 [\(1992\)](#); [Hauser et al. \(2008, 1992\)](#); [Caudal et al. \(2014\)](#)), which are designed for the mea-  
714 surements of wave directional spectrum, can also measure 2-D scattering coefficient as a  
715 function of incident angle and azimuthal angle of 0-360°. In the near future (2018), the  
716 SWIM (Surface Waves Investigation and Monitoring) radar, which will be carried on the  
717 CFOSAT (China-France Oceanography Satellite) will provide simultaneously the normal-  
718 ized radar backscatter at near-nadir incidence in a 2-D geometry and 2-D spectra of ocean  
719 dominant waves. Hence, it will give new opportunities to further study the relationship  
720 between the slope PDF parameters and the wind and long waves. Future work using a large  
721 data set from satellite should also be used in combination with external data from models  
722 or in situ measurements to assess the impact of atmospheric stability on peakedness of the  
723 slope PDF ([Shaw and Churnside \(1997\)](#); [Longuet-higgins \(1982\)](#); [Mc Daniel \(2003\)](#)).

724 The result presented here on the non-Gaussian slope PDF are associated to Ku-band  
725 conditions and cannot be generalized to other conditions because of remaining filtering effects  
726 which depend in electromagnetic wavelength, even if they are smaller than when using a  
727 Quasi-specular model for the inversion. However, the main trends with wind speed and  
728 wave conditions found here may be more general since for all parameters, we find trends  
729 which are intermediate between the optical limit (Cox and Munk clean sea and slick sea  
730 case). Analysis of Ka-band data with the approach proposed here will be of particular  
731 interest because we expect to be close to the optical limit where all scales account.

## 732 **7. Acknowledgments**

733 The authors would like to thank Professor Yijun He and Researcher Xiaoqing Chu for  
734 providing the PR data set matched with NDBC buoy, and thank Dr. Charles-Antoine  
735 Guerin and Dr. F. Nouguier for giving some important suggestions to our work. The

736 authors greatly appreciate the anonymous reviewers for their detailed comments that helped  
 737 to improve the manuscript. This work was supported in part by the National Key Research  
 738 and Development Program of China (2016YFC1401005), by the Open Fund of the State Key  
 739 Laboratory of Satellite Ocean Environment Dynamics (SOED1607).

## 740 8. Appendixes

741 In order to examine the effect of frequency on the performance of inv-GO4, Fig.A1  
 742 and Fig.A2 show  $\sigma^0(\theta)$  calculated with PO, inv-GO4 and QS for C-band and Ka-band,  
 743 respectively, with EL spectrum ( $U=10$  m/s). Color codes and symbols are the same as in  
 744 Fig.1.

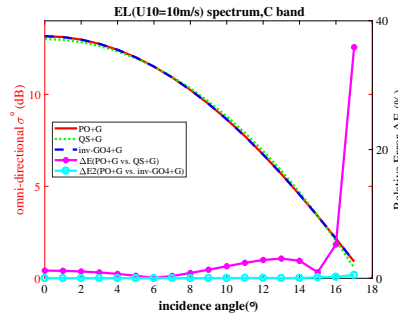


**Fig. A1.**  $\sigma^0(\theta)$  (in dB) as a function of  $\theta$  with the PO model (red line) for a 10 m/s wind speed, using EL spectrum, for C-band. Color codes and symbols are the same as in Fig.1

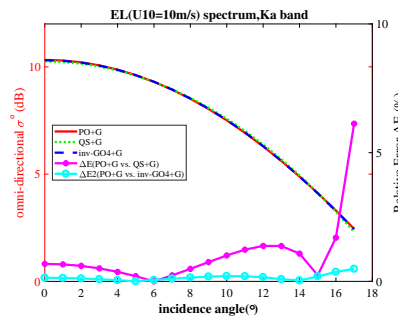


**Fig. A2.**  $\sigma^0(\theta)$  (in dB) as a function of  $\theta$  with the PO model (red line) for a 10 m/s wind speed, using EL spectrum, for Ka-band. Color codes and symbols are the same as in Fig.1

745 **References**

- 746 Barrick, D. E., 1968. Relationship between slope probability density function and the physical  
747 optics integral in rough surface scattering. *Proceedings of the IEEE* 56 (10), 1728–1729.
- 748 Boisot, O., Noguier, F., Chapron, B., Guèrin, C. A., 2015. The go4 model in near-nadir  
749 microwave scattering from the sea surface. *IEEE Transactions on Geoscience and Remote*  
750 *Sensing* 53 (11), 5889–5900.
- 751 Brèon, F. M., Henriot, N., 2006. Spaceborne observations of ocean glint reflectance and  
752 modeling of wave slope distributions. *Journal of Geophysical Research Oceans* 111 (C6),  
753 C06005.
- 754 Bringer, A., Guerin, C. A., Chapron, B., Mouche, A. A., 2012. Peakedness effects in near-  
755 nadir radar observations of the sea surface. *IEEE Transactions on Geoscience and Remote*  
756 *Sensing* 50 (9), 3293–3301.
- 757 Caudal, G., Dinnat, E., Boutin, J., 2005. Absolute calibration of radar altimeters: Con-  
758 sistency with electromagnetic modeling. *Journal of Atmospheric and Oceanic Technology*  
759 22 (6), 771–781.
- 760 Caudal, G., Hauser, D., Valentin, R., Gac, C. L., 2014. Kuros: A new airborne ku-band  
761 doppler radar for observation of surfaces. *Journal of Atmospheric and Oceanic Technology*  
762 31 (10), 2223–2245.
- 763 Center, E. O., 2001. TRMM data users handbook. National Space Development Agency of  
764 Japan.
- 765 Chapron, B., Kerbaol, V., Vandemark, D., Elfouhaily, T., 2000. Importance of peakedness in  
766 sea surface slope measurements and applications. *Journal of Geophysical Research Oceans*  
767 105 (C7), 17195C17202.
- 768 Chu, X., 2011. The algorithm and applied basic study on remote sensing of ocean wave  
769 spectrum for ocean wave spectrometer. Ph.D. thesis, Chinese Academy of Sciences.

770 Chu, X., He, Y., Chen, G., 2012a. Asymmetry and anisotropy of microwave backscatter  
771 at low incidence angles. *IEEE Transactions on Geoscience and Remote Sensing* 50 (10),  
772 4014–4024.

773 Chu, X., He, Y., Karaev, V. Y., 2012b. Relationships between ku-band radar backscatter  
774 and integrated wind and wave parameters at low incidence angles. *IEEE Transactions on*  
775 *Geoscience and Remote Sensing* 50 (11), 4599–4609.

776 Cox, C., Munk, W., Nov 1954. Measurement of the roughness of the sea surface from pho-  
777 tographs of the sun’s glitter. *J. Opt. Soc. Am.* 44 (11), 838–850.

778 Cox, C. S., Munk, W. H., 1956. Slopes of the sea surface deduced from photographs of sun  
779 glitter. *Bull.scripps Inst.oceanogr* 6.

780 Durden, S. L., Vesecky, J. F., 1985. A physical radar cross-section model for a wind-driven  
781 sea with swell. *IEEE Journal of Oceanic Engineering* 10 (4), 445–451.

782 Elfouhaily, T., Chapron, B., Katsaros, K., Vandemark, D., 1997. A unified directional spec-  
783 trum for long and short wind driven waves 102 (C7), 15.

784 Freilich, M. H., Vanhoff, B. A., 2003. The relationship between winds, surface roughness, and  
785 radar backscatter at low incidence angles from trmm precipitation radar measurements.  
786 *Journal of Atmospheric and Oceanic Technology* 20 (4), 549–562.

787 Hauser, D., Caudal, G., Guimbard, S., Mouche, A. A., 2008. A study of the slope probability  
788 density function of the ocean waves from radar observations 113 (C2), 710–713.

789 Hauser, D., Caudal, G., Rijckenberg, G. J., Vidal-Madjar, D., Laurent, G., Lancelin, P.,  
790 1992. Ressac: a new airborne fm/cw radar ocean wave spectrometer. *IEEE Transactions*  
791 *on Geoscience and Remote Sensing* 30 (5), 981–995.

792 Hesany, V., Plant, W. J., Keller, W. C., 2000. The normalized radar cross section of the sea  
793 at 10 incidence. *Geoscience and Remote Sensing IEEE Transactions on* 38 (1), 64–72.



- 794 Hwang, P. A., 2005. Wave number spectrum and mean square slope of intermediate-scale  
795 ocean surface waves. *Journal of Geophysical Research Oceans* 110 (C10), 9.
- 796 Hwang, P. A., Wang, D. W., 2004. An empirical investigation of source term balance of small  
797 scale surface waves. *Geophysical Research Letters* 31 (15), 121–141.
- 798 Jackson, F. C., Travis, W. W., Peng, C. Y., 1985. A comparison of in situ and airborne radar  
799 observations of ocean wave directionality 90 (NC1), 1005andndash;1018.
- 800 Jackson, F. C., Walton, W. T., Hines, D. E., Walter, B. A., Peng, C. Y., 1992. Sea sur-  
801 face mean square slope from ku-band backscatter data. *Journal of Geophysical Research:*  
802 *Oceans* 97 (C7), 11411–11427.  
803 URL <http://dx.doi.org/10.1029/92JC00766>
- 804 Klein, L., Swift, C., 1977. An improved model for the dielectric constant of sea water at  
805 microwave frequencies. *IEEE Transactions on Antennas & Propagation* 2 (1), 104–111.
- 806 Longuet-Higgins, M. S., 1978. *On the Dynamics On the Skewness of Steep Gravity Waves in*  
807 *Deep Water*. Springer US.
- 808 Longuet-higgins, M. S., 1982. On the skewness of sea-surface slopes. *Journal of Physical*  
809 *Oceanography* 12 (11), 1283–1291.
- 810 Mc Daniel, S. T., 2003. Microwave backscatter from non-gaussian seas. *IEEE Transactions*  
811 *on Geoscience and Remote Sensing* 41 (1), 52–58.
- 812 Om, P., 1985. Spectral and statistical properties of the equilibrium range in wind generated  
813 gravity waves. *Journal of Fluid Mechanics* 156 (-1), 505–531.
- 814 Ping Chen, Q. Y., Huang, P., 2015. Effect of non-gaussian properties of the sea surface on  
815 the low-incidence radar backscatter and its inversion in terms of wave spectra by an ocean  
816 wave spectrometer. *Journal of Oceanology and Limnology* 33 (5), 1142–1156.

817 Resio, D., Perrie, W., 02 1991. A numerical study of nonlinear energy fluxes due to wave-wave  
818 interactions part 1. methodology and basic results. Journal of Fluid Mechanics 223 (-1),  
819 603–629.

820 Shaw, J. A., Churnside, J. H., Jun 1997. Scanning-laser glint measurements of sea-surface  
821 slope statistics. Appl. Opt. 36 (18), 4202–4213.  
822 URL <http://ao.osa.org/abstract.cfm?URI=ao-36-18-4202>

823 Thompson, D. R., Elfouhaily, T. M., Garrison, J. L., 2005. An improved geometrical optics  
824 model for bistatic gps scattering from the ocean surface. IEEE Transactions on Geoscience  
825 and Remote Sensing 43 (12), 2810–2821.

826 Tsang, L., Kong, J. A., 2001. Scattering of Electromagnetic Waves, Advanced Topics. Wiley.

827 Vandemark, D., Chapron, B., Sun, J., Crescenti, G. H., Graber, H. C., 2004. Ocean  
828 wave slope observations using radar backscatter and laser altimeters. Journal of Physical  
829 Oceanography 34 (12), 2825–2842.

830 Wu, J., 1972. Sea surface slope and equilibrium wind wave spectra 15 (5), 741–747.

831 **List of Figures**

832 Figure 1: The value of  $\sigma^\circ(\theta)$  using EL spectrum for Ku-band..... 10

833 Figure 2: the value of  $\sigma^\circ(\theta)$  using EL spectrum combined with swell spectrum ..... 11

834 Figure 3: The inverted  $mss$  and  $mss$  by inv-GO4 model ..... 17

835 Figure 4: The inverted  $mss$ ,  $mssx$  and  $mssy$  by inv-GO4 model..... 17

836 Figure 5: The inverted  $mssx$ ,  $mssy$  and  $mssxy$  by inv-GO4 model..... 18

837 Figure 6: The inverted fresnel coefficient by inv-GO4 model..... 19

838 Figure 7: The data number under different wind speed and relative wind direction..... 21

839 Figure 8: Relative inversion error under different wind speeds..... 24

840 Figure 9: The inverted  $mss$ ,  $mssx$  and  $mssy$  by inv-GO4 model with PR data ..... 26

841	Figure 10:	The inverted skewness coefficients by inv-GO4 model with PR data .....	27
842	Figure 11:	Effect of wind vs. wave direction on skewness coefficients .....	28
843	Figure 12:	The inverted peakedness coefficients by inv-GO4 model with PR data.....	29
844	Figure 13:	Effect of wind vs. wave direction on peakedness coefficient.....	30
845	Figure 14:	Slope PDF in upwind and crosswind directions.....	33
846	Figure A1:	The value of $\sigma^\circ(\theta)$ using EL spectrum for C-band .....	37
847	Figure A2:	The value of $\sigma^\circ(\theta)$ using EL spectrum for Ka-band.....	37